GENESIS AND GEODYNAMIC EVOLUTION OF SERPENTINIZED ULTRAMAFICS AND ASSOCIATED MAGNESITE DEPOSITS IN THE AL-WASK OPHIOLITE, ARABIAN SHIELD, SAUDI ARABIA

HISHAM A. GAHLAN*,**, MOKHLES K. AZER***, PAUL D. ASIMOW§,†, and KHALED M. AL-KAHTANY§§

ABSTRACT.   Situated along the Yanbu Suture Zone, the Al-Wask ophiolite is one of the largest and best-preserved ophiolite sequences in the Proterozoic Arabian shield. A mantle section of serpentinized ultramafics is structurally overlain by a crustal section of gabbros and pillow lavas. The whole ophiolite sequence is capped by pelagic sedimentary cover, and tectonically emplaced over a metamorphosed island-arc volcano-sedimentary succession. The Al-Wask ultramafic rocks are strongly deformed, metamorphosed, and altered by carbonatization and silicification. Samples dominated by antigorite indicate upper greenschist to lower amphibolite facies peak metamorphic grade, whereas samples dominated by lizardite and magnesite preserve lower grade conditions that we interpret as a cooling path buffered to low CO_2 activity by the increasing stability of magnesite with decreasing temperature. Nearly all the primary silicate minerals have been replaced by serpentine minerals, leaving only relics of primary olivine and chromian spinel. Petrographic observation of relict olivine and spinel and of mesh and bastite textures in the serpentines suggest that the peridotite protoliths were mainly harzburgite with minor dunite. Whole-rock compositions of serpentinites show low CaO (<0.1 wt.%), Al_2O_3 (<1.5 wt.%), and Y (<0.4 ppm) combined with high Mg# (0.90–0.92), Ni, Co, and Cr contents; all these indicate a highly refractory mantle protolith. The mineral chemistry of relict primary spinel and olivine provides additional petrogenetic and geodynamic indicators. The high Cr# (> 60) and low TiO_2 (≤0.2 wt. %) of spinel and high forsterite contents (90–92) of associated olivine indicate residual mantle that underwent extensive partial melt extraction. The whole-rock and mineral chemistry of the serpentinized ultramafic rocks are both consistent with extracted melt fractions from ~32 to 38 percent. This extent of melting is typical of fore-arc supra-subduction zone settings, which is the most likely tectonic environment for formation and preservation of the Al-Wask ophiolite.

Two types of magnesite deposits can be distinguished in the Al-Wask mantle section: an early generation of massive magnesite and a later generation of magnesite veins. Hence the Al-Wask ophiolite underwent multiple stages of carbonatization, likely involving different sources of CO_2-bearing fluids. The massive magnesite likely formed at relatively high temperature during cooling from peak metamorphic condition from CO_2-bearing fluid probably derived from decomposition of subducted carbonates. Using thermodynamic calculations in the simple MgO-SiO_2-H_2O-CO_2 system, we constrain the path of the reaction boundary where lizardite and magnesite can coexist at equilibrium. On the other hand, the cryptocrystalline magnesite veins fill tectonic fractures and likely formed at low temperature and shallow levels, after serpentinization and ophiolite obduction.

Keywords: Al-Wask ophiolite, mantle, magnesite, supra-subduction zone, Arabian Shield

* Department of Geology and Geophysics, King Saud University, Riyadh 11451, Saudi Arabia
** Geology Department, Assiut University, Assiut 71516, Egypt
*** Geological Sciences Department, National Research Centre,12622-Dokki, Cairo, Egypt
§ Division of Geological & Planetary Sciences, California Institute of Technology, Pasadena, California 91125, USA
§§ Seismic Studies Center, College of Science, King Saud University, Riyadh 11451, Saudi Arabia
† Corresponding author: asimow@gps.caltech.edu

Ophiolites are fragments of oceanic lithosphere, tectonically emplaced onto continental margins during the closure of ocean basins. These sequences consist of a lower "mantle" unit of serpentinized ultramafic rocks and an upper "crustal" unit of layered and isotropic gabbro, sheeted dikes and pillow basalts (Coleman, 1977; Stern and others, 2004; Johnson and others, 2004). They may have formed in a variety of tectonic settings, associated with both divergent margins (mid-ocean ridges) and convergent margins (subduction systems) (for example, Dilek and others, 2008; Dilek and Furnes, 2011, 2014; Furnes and others, 2014). Accordingly, ophiolites can record the paleotectonic history of oceanic lithosphere. Although there are numerous well-preserved and intact Phanerozoic-aged ophiolites, those of Precambrian age are typically dismembered, altered and metamorphosed to various extents.

The Arabian-Nubian Shield (ANS) formed in the Neoproterozoic between *ca.* 870 and *ca.* 540 Ma (Stern, 1994) and, especially in the Arabian Shield, a number of ophiolite sequences were obducted during its amalgamation. The ANS ophiolites (*ca.* 870–690 Ma; Stern and others, 2004; Ali and others, 2010) are of great importance for defining the shield's crustal growth and the events of the Pan-African orogeny, yet the Arabian Shield ophiolite occurrences remain comparatively under studied.

Conspicuous within the ophiolites of the Arabian Shield is the abundance of carbonate-altered ultramafic rocks. Altered ultramafic rocks in the ophiolites of the Arabian Shield include serpentinite, talc-carbonate rocks, magnesite and several varieties of listvenite (Stern and others, 2004; Johnson and others, 2004). Although carbonate-altered ultramafic rocks have been known in the Saudi basement complex for many years, the process or processes that caused the carbonation and other effects related to these processes remain poorly studied and understood. The large volume of carbonated rocks implies significant fluxes of CO_2-bearing fluids — fluxes that might have occurred (in principle) before, during, or after the Late Neoproterozoic (~600 Ma) amalgamation of the ANS. The origin of these CO_2-bearing fluids in the Arabian Shield has not been studied in detail.

Carbonate-altered rocks are spatially associated with magnesite veins and host shear zones that serve as focused areas for development of talc, gold (Botros, 2002), and garnierite deposits (Hamdy and Gamal El Dien, 2017). Hence the scientific objective of studying the Arabian Shield ophiolites is closely linked to the economic objective of understanding the relative roles of the ophiolite itself and of externally-derived fluids that infiltrated the ophiolite in determining the type and location of ore deposits within ultramafic-hosted metallogenic provinces.

The Al-Wask ophiolite belt (Western Arabian Shield, Saudi Arabia) is one of the most famous ophiolitic occurrences in the Arabian Shield, yet no detailed petrological studies have described the geochemical and mineralogical characteristics of this important ophiolite suite. This is the first detailed geochemical and mineralogical investigation of the mantle section of the Al-Wask ophiolite. We integrate field observations, petrography, whole-rock and mineral chemistry in order to discern the petrological characteristics and geodynamic setting of the Al-Wask ophiolite. We furthermore offer a characterization of the carbonate alteration products and economically viable deposits of the industrial mineral magnesite in the Al-Wask ophiolite.

GEOLOGIC SETTING

The Neoproterozoic ophiolites of the Arabian Shield (AS) are fragments of oceanic lithosphere obducted onto continental crust during closure of the Mozambique Ocean and collision between West and East Gondwana (for example, Pallister and others, 1988; Stern, 1994; Dilek and Ahmed, 2003; Stern and others, 2004). Many AS ophiolites lie along large faults and major shear zones and demarcate the sutures between terranes of different lithostratigraphy (fig. 1). The AS ophiolites are typically
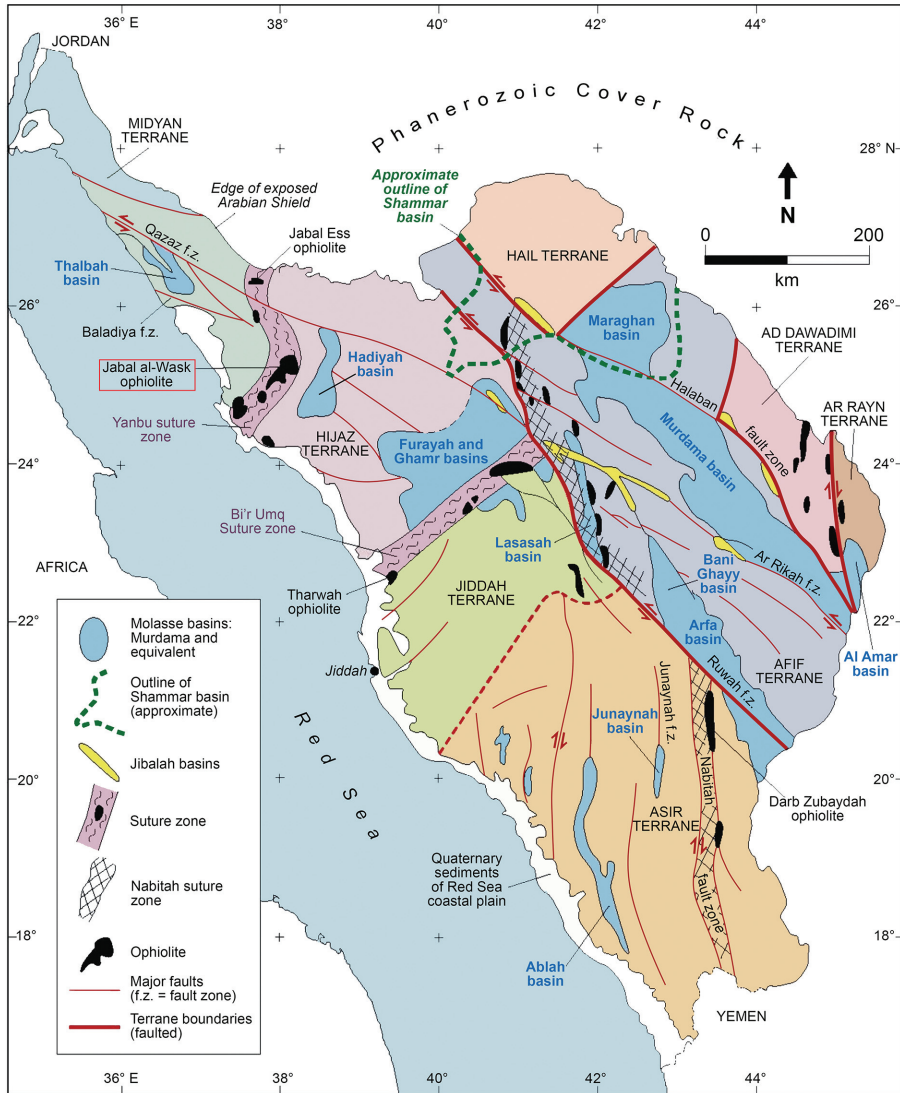
Fig. 1. Regional tectonic map of the Arabian Shield showing suture zones hosting ophiolite sequences in western Saudi Arabia (Nehlig and others, 2002).

dismembered and have suffered multiple phases of alteration, deformation and metamorphism (Al-Shanti and Gass, 1983; Nassief and others, 1984; Ahmed and Hariri, 2008; Habtoor and others, 2017).

The Al-Wask (also spelled Al Wasq) ophiolite outcrops in the central part of the Yanbu suture (fig. 1), a NE-oriented belt that extends from the north-western AS into northeast Africa (for example, Abdelsalam and Stern, 1996; Abdelsalam and others, 2003; Johnson and Woldehaimanot, 2003; Ali and others, 2010). Stern and others (1990) named this extended series of suture structures (Yanbu–Onib–Sol Hamed–Gerf–Allaqi–Heiani) the YOSHGAH suture. The YOSHGAH suture zone is typically about 50 km wide and consists of gneisses, ophiolites, island arc metavolcanic-metasedimentary

Fig. 2. Geologic map indicating outcrop area of the Al-Wask ophiolite and its country and cover rocks, modified after Hadley (1987).
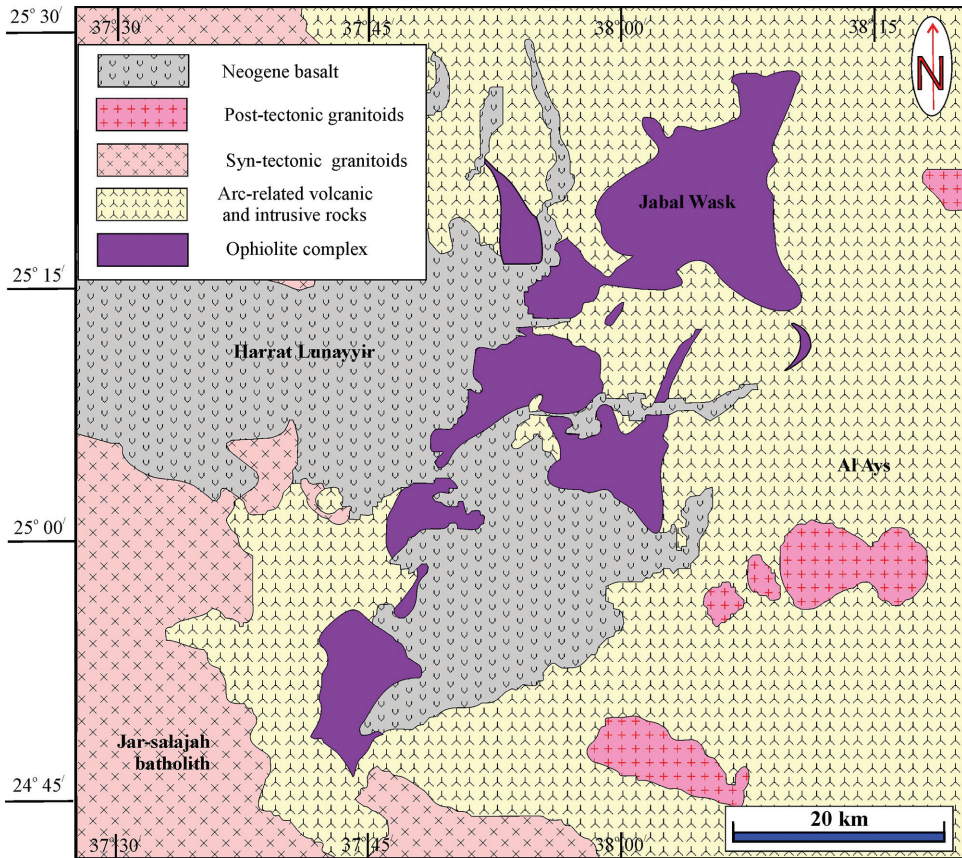
successions and gabbroic to granitic intrusions (for example, Kröner and others, 1992; Abd El-Naby and Frisch, 2002; Kusky and Ramadan, 2002; Abdelsalam and others, 2003; Ali and others, 2010; Azer and others, 2013). The Yanbu segment of the YOSHGAH suture separates the Midyan and Hijaz microplates in northwestern Saudi Arabia and includes the Jabal Al-Wask and Jabal Ess ophiolites, which yield model ages of 740 to 780 Ma (Pallister and others, 1988).

The Al-Wask ophiolite complex is one of the largest and best-preserved ophiolite sections in the AS (for example, Al-Shanti, ms, 1982; Pallister and others, 1988; Johnson and others, 2004). It lies between latitudes 24º 45′ and 25º 30′ N and longitudes 37º 30′ and 38º 15′ E (fig. 2), extending about 80 km from northeast to southwest, parallel to the general structural fabric of the Yanbu Suture. The ophiolite forms a series of folded thrust sheets intercalated with a group of Late Neoproterozoic arc-related volcanic and sedimentary successions and granitoids. The area is unconformably overlain by the Neogene Harrat Lunayyir plateau basalts.

The Al-Wask ophiolite is dominated by the lower units of the lithologic sequence that defines a classic Penrose-type ophiolite suite (fig. 3; Penrose Conference Participants, 1972). Most contacts between the different rock units are structural (faults). An extensive mélange zone accompanies the sole thrust at the base of the sequence. The
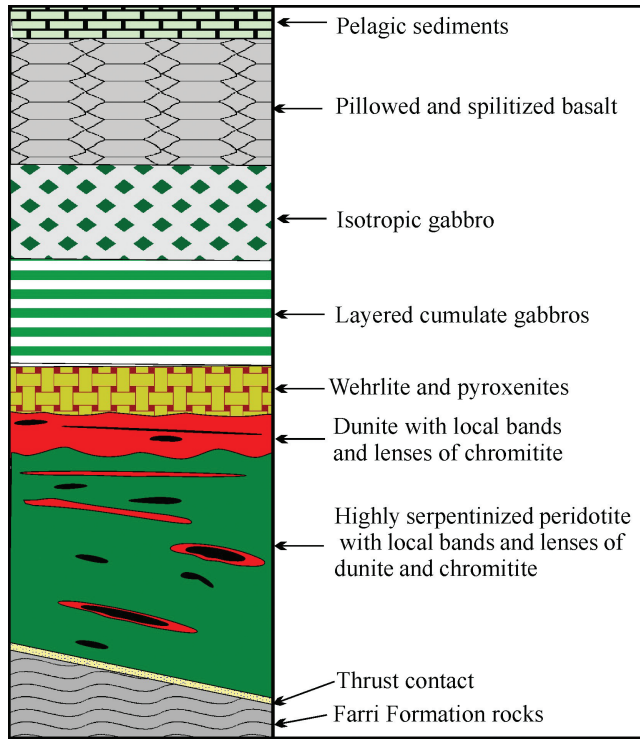
Fig. 3. Schematic lithostratigraphic section of the Al-Wask ophiolite (not to scale).

mélange consists mainly of metagabbro and metavolcanic blocks entrained in a serpentinite matrix. A mantle section of serpentinized ultramafic rocks is overlain by a crustal section of gabbros and pillow lavas. The pelagic sediments cap the sequence. Notably, sheeted dikes have not been recognized. The Al-Wask ultramafic rocks are highly serpentinized, deformed and mylonitized. Serpentinized harzburgite is the dominant rock type, while serpentinized dunite is less common. Chromitite, though scarce, forms small pods and lenticular layers often enveloped by serpentinized ultramafics, with both massive and disseminated textures.

Extensive mylonitization and carbonatization are associated with major tectonic lineaments and faults cutting the ophiolite. This post-emplacement deformation is probably connected with reactivation of the Najd fault system (Stern, 1985; Agar, 1987; Kusky and Matsah, 2003). In the study area, subvertical shear zones are defined by serpentinite schist, listvenite, magnesite, and mélange (fig. 4A). Along shear zones and fault planes, ultramafic rocks are largely altered to talc-carbonates, magnesite and listvenite (fig. 4B). In places, the Neogene Harrat Lunayyir basalt flowed directly over exposed serpentinite outcrop (fig. 4C).

Magnesite bodies are commonly hosted by serpentinite, most often at contacts with country rocks and along regional faults. Magnesite forms masses, pockets and snow-white veins, all with sharp but irregular boundaries (figs. 4D and 4E). It is very hard and sometimes variably stained with iron oxides. The magnesite veins vary from microscale networks infiltrating the serpentinite matrix through cm-scale and up to a maximum width of 0.5 m. The magnesite veinlets are generally concordant to foliation in the sheared serpentinites, and rarely pass gradually into magnesite stockworks. Serpentinite rock fragments can be observed enclosed in some of the magnesite masses.
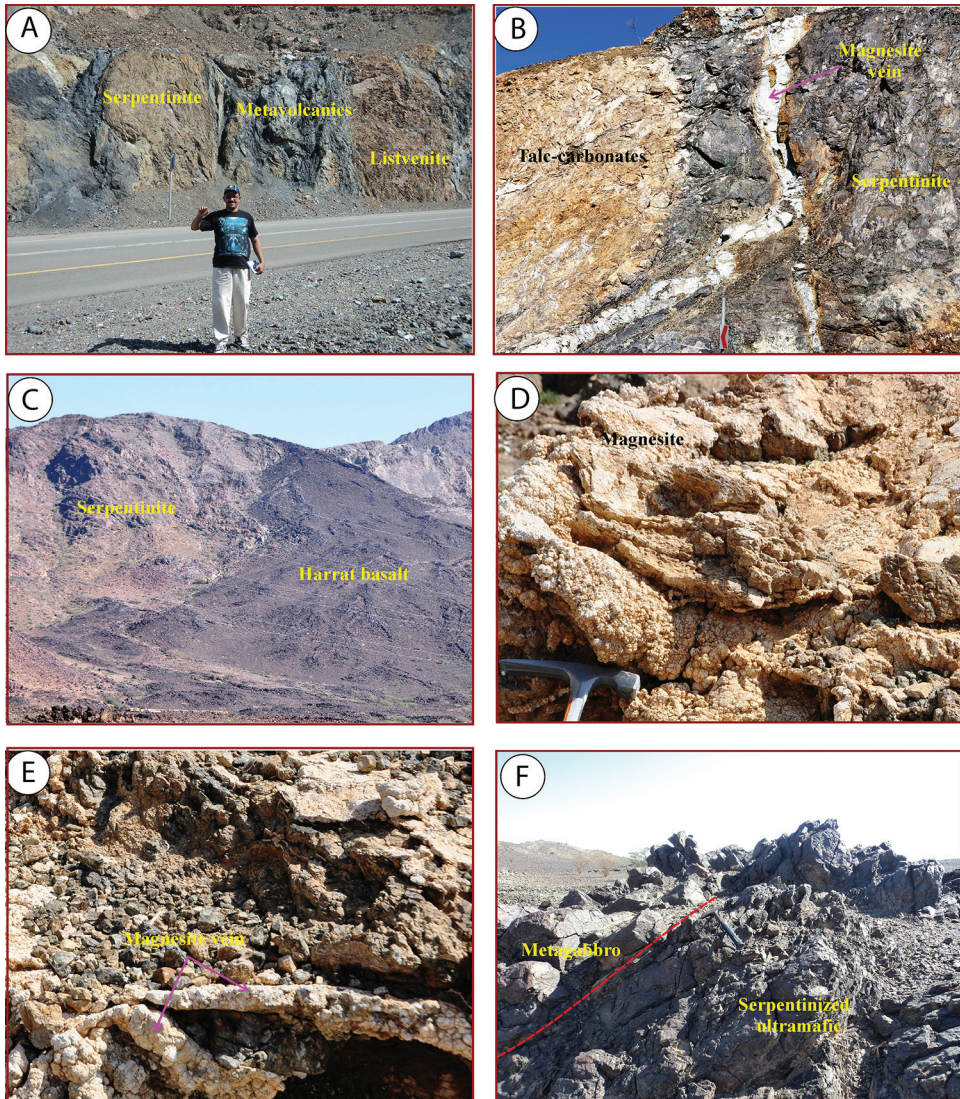
Fig. 4. Field photos of the Al-Wask ophiolite, Arabian Shield, Saudi Arabia; (A) ophiolitic mélange along the sole thrust of the sequence, with blocks of serpentinite, listvenite and metavolcanic rock; (B) talc-carbonate and magnesite along a shear zone; (C) Neogene Harrat Lunayyir basalt unconformably overlying serpentinite; (D) massive magnesite with serpentinite; (E) magnesite veins within a shear zone; and (F) metagabbro overlying serpentinized ultramafic rocks.

Listvenite bodies of various shapes and sizes developed by alteration of ultramafic rocks, particularly along shear zones. Reddish-brown in color and resistant to erosion, the Al-Wask listvenites form prominent ridges along major shear zones and fault planes or within mélange zones. In poorly exposed areas, the presence of ridges of listvenite may be the only evidence for underlying mafic-ultramafic rocks.

A normal thickness (up to 2 km; Stern and others, 2004) of metagabbro overlies the ultramafic cumulates with typically sheared or structural contacts (fig. 4F). Modally layered gabbros constitute a very thin zone, exposed only at few localities; the bulk of

the crustal section is isotropic gabbro. The metagabbros grade upwards from pyroxene-rich to hornblende-rich varieties, with minor diorites throughout. Spilites, sparse metasediments, and metatuffs overlie the metagabbro.

PETROGRAPHY AND MINERALOGY

Serpentinized Ultramafic Series

The ultramafic rocks of the Al-Wask ophiolite are almost completely serpentinized; harzburgite is the most dominant mantle lithology, followed by dunite and chromitite. In thin section, samples consist essentially of serpentine minerals (> 90%) with variable amounts of carbonates, talc and magnetite and minor amphibole and chlorite. Most samples include relics of fresh olivine and chromian spinel. We confirmed the specific identity of the serpentine minerals using both whole-rock powder X-ray diffraction and *in situ* Raman spectroscopy, examining both the low-wavenumber (silicate structure vibrations) and high-wavenumber (hydrogen species vibrations) regions (Petriglieri and others, 2015). The serpentine mineralogy varies from sample to sample. Some samples are dominated by antigorite with minor veinlets of chrysotile. The antigorite forms plates and fibers with interlocking to interpenetrative textures or scaly aggregates (fig. 5A). The veinlets of chrysotile cross-cut the fibers of the antigorite matrix (fig. 5B). The antigorite-rich samples have only minor magnesite. In other samples all the serpentine is lizardite, forming elongated fibrous crystals, sometimes agglomerated into bundles. The lizardite-rich samples have abundant magnesite. Serpentinites, particularly the antigorite-dominated samples, commonly preserve the original texture and crystal habits of orthopyroxene and olivine, indicating harzburgite and dunite protoliths. Original crystals of orthopyroxene are marked by bastite texture, with thin magnetite striations decorating the cleavage planes of the original orthopyroxene (fig. 5C). Pervasive mesh texture after olivine indicates dunite parentage (fig. 5D). Mesh zones occasionally feature olivine relics in the centre and iron oxides along the rims (fig. 5E).

The fresh relics of primary olivine form anhedral strained and cracked crystals dissected by networks of serpentine in interlocking textures (fig. 5E). In massive serpentinite, chromian spinel forms subhedral to euhedral crystals, whereas in sheared serpentinite the chromian spinel is mostly brecciated. Sometimes, chromian spinel is partly replaced by ferritchromite and magnetite around its rim (fig. 5F). Carbonates occur as patches, sparse crystals and fine aggregates. Magnetite occurs as disseminated crystals, fine opaque clusters surrounding olivine crystals, rims on spinel, and inclusions in bastite. Traces of tremolite are observed in a few samples as fibrous aggregates with strong birefringence embedded in serpentine matrix. Minor chlorite occurs as fine aggregates or scattered flakes intermixed with serpentine minerals. Traces of talc occur as fine anhedral aggregates or as microcrystalline fibers associated with carbonates.

Magnesite

In addition to the disseminated magnesite principally found in lizardite-rich serpentinite specimens, magnesite forms nearly pure (> 97 vol. %) veins and irregular masses. The vein magnesite is cryptocrystalline and anhedral. Minor phases in magnesite bodies include serpentine minerals, chrome spinel and iron oxides, sometimes in the form of angular fragments of host serpentinite within the massive magnesite (fig. 5G). Chromian spinel is anhedral and highly altered to magnetite (fig. 5H). Rare coarse crystals of dolomite and calcite can be observed in a few samples and a few quartz veinlets are found in the massive magnesite. The magnesite masses display evidence of shearing via recrystallization along grain boundaries and stretched grain ribbons.

MINERAL CHEMISTRY

Primary fresh relics of olivine and chrome spinel as well as secondary minerals (serpentine, amphibole and chlorite) were analyzed for mineral chemistry by electron
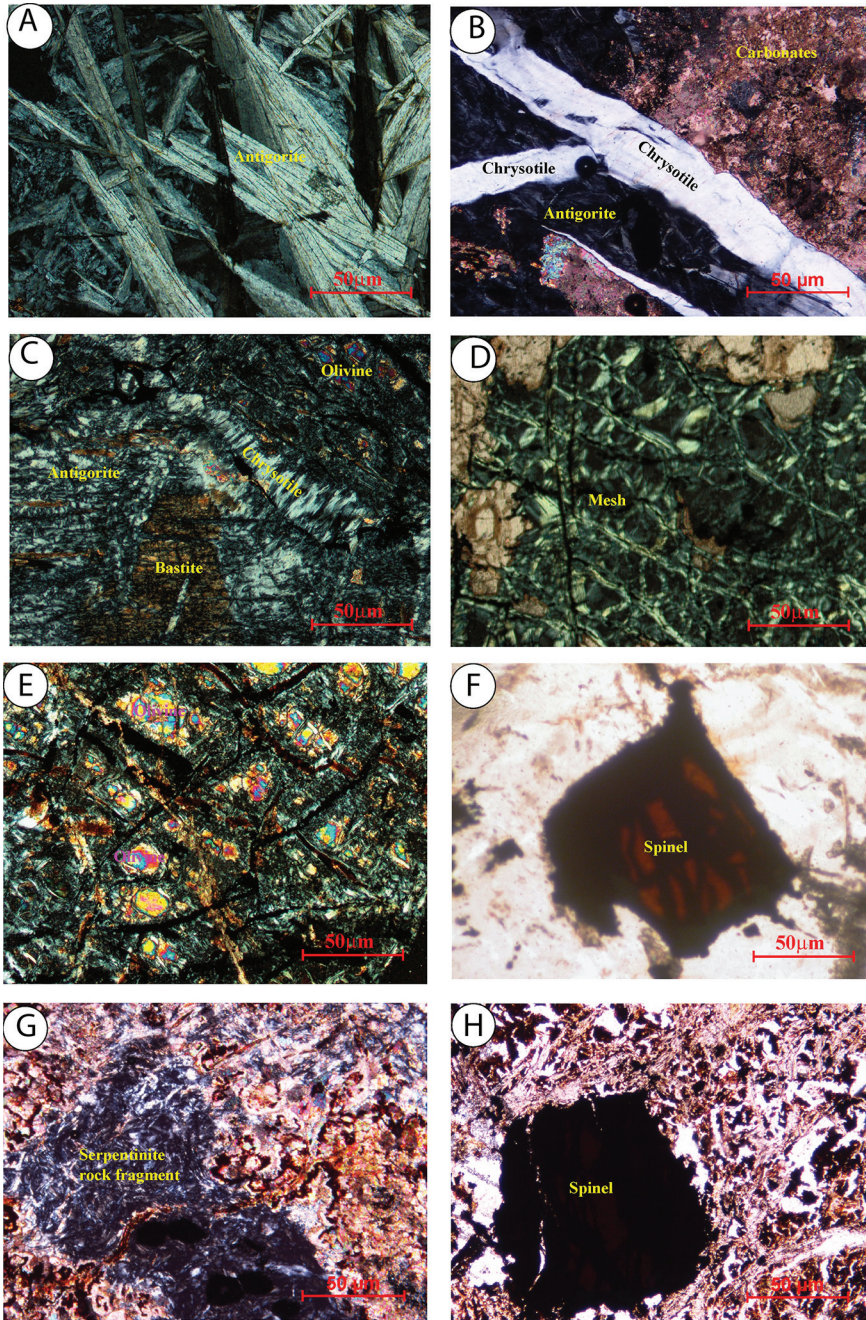
Fig. 5. Photomicrographs showing petrographic textures. All photos are taken in crossed polarized light, except that (f) and (h) are plane polarized transmitted light images. (A) Fibrolamellar aggregates of antigorite in sample W57, (B) chrysotile veinlets cutting antigorite and carbonates in sample W22, (C) bastite texture and fresh olivine relics within serpentine minerals in sample W52, (D) mesh texture with dispersed crystals of magnesite in sample W37, (E) fresh olivine relics within a matrix of serpentine minerals in sample W40, (F) chromian spinel crystal altered along the margins and cracks to ferritchromite in sample W57, (G) angular fragment of serpentinite within massive magnesite in sample W8, (H) ferritchromite with fresh core of chromian spinel in sample W43.

microprobe. The five-spectrometer JEOL JXA-8200 instrument in the Division of Geological and Planetary Sciences at the California Institute of Technology was operated at 15 kV accelerating voltage with a focused (~1 μm diameter) 25 nA beam. Each peak was counted for 20 seconds and high and low background positions were counted for 10 seconds each. Primary standards included synthetic (anorthite for Ca and Al; forsterite for Si and Mg; fayalite for Fe; Mn-olivine for Mn; NiO for Ni; Cr_2O_3 for Cr; TiO_2 for Ti) and natural (Amelia albite for Na; Asbestos microcline for K) minerals. Complete data are given in Appendix tables A1-A8 and are duplicated in the supplement tables 1S-8S (http://earth.geology.yale.edu/%7eajs/SupplementaryData/2020/Gahlan).

Olivine

Fresh primary olivine relics were analyzed in both serpentinized harzburgite and dunite. Chemical analyses and calculated structural formulae and end-member proportions of olivine are given in Appendix tables A1 and A2 and in supplementary data tables 1S and 2S. All measured olivine is unzoned forsterite with a relatively narrow compositional range in each rock type. Olivine in dunite has higher MgO content (49.21–51.47 wt.%; av. 50.22) than in harzburgite (48.56–49.92 wt.%; av. 49.45). Fo content ranges from 89 to 91 (av. 90) in harzburgite and from 91 to 93 (av. 92) in dunite. Despite some overlap, NiO contents are generally higher in olivine from dunite (0.39–0.52 wt.%) than in harzburgite (0.34–0.46 wt.%). Both groups lie in the range of the olivine mantle array (fig. 6A). All the analyzed olivines have negligible (with this analytical protocol) amounts of TiO_2 (< 0.02 wt. %), Cr_2O_3 (< 0.06 wt. %), Al_2O_3 (< 0.02 wt. %), and CaO (< 0.07 wt. %).

The NiO and Fo contents of primary olivine from both harzburgite and dunite in the Al-Wask mantle section are similar to typical mantle olivine compositions (Takahashi and others, 1987) and to previously reported primary olivine from other ophiolitic peridotites in the ANS (for example, Pallister and others, 1988; Ahmed and Habtoor, 2015; Gahlan and others, 2018; Azer and others, 2019) (fig. 6A). However, Fo and NiO contents are distinctly higher than in olivine from non-ophiolitic mafic-ultramafic intrusions throughout the ANS (for example, Khudeir, 1995; Helmy and El-Mahallawi, 2003; Farahat and Helmy, 2006; Azer and El-Gharbawy, 2011; Azer and others, 2016, 2017).

Chromian Spinel

Chromian spinel was analyzed in both serpentinized ultramafic and massive magnesite samples. The compositions and structural formulae of spinel-group minerals are given in Appendix tables A3-A5 and supplementary tables 3S (harzburgite), 4S (dunite), and 5S (magnesite masses). Most of the analyzed spinel grains have fresh Cr-spinel cores with altered rims consisting of an inner zone of ferritchromite and an outer zone of Cr-magnetite. In magnesite masses, Cr-magnetite may be the only alteration product around Cr-spinel. Fresh spinel cores are rich in Al_2O_3, Cr_2O_3 and MgO; FeO^T systematically increases outwards. On an Al–Cr–Fe^{3+} triangular plot (fig. 6B), ferritchromite and Cr-magnetite plot along or close to the Cr–Fe^{3+} join, whereas fresh Cr-spinels plot close to the Cr–Al join. Evidently, alteration and metamorphism are marked by increases in Fe_2O_3 (as FeO^T); the well-defined Fe-rich overgrowth rims indicated that, most likely, the addition of Fe increased the molar proportion of spinel and magnetite in the rocks, diluting Al and Cr contents, rather than substituting for those elements in a rock with a constant proportion of the spinel phase. All fresh Cr-spinel cores have low Fe^{3+}# [$Fe^{3+}/(Fe^{3+}+Cr+Al)$], <0.09, which is considered to be a diagnostic feature of primary mantle-derived spinel (for example, Dick and Bullen, 1984; Irvine, 1965, 1967; Hattori and Guillot, 2007; Bernstein and others, 2013). The Fe^{3+}# in the Al-Wask samples resembles that in Cr-spinel from ophiolitic
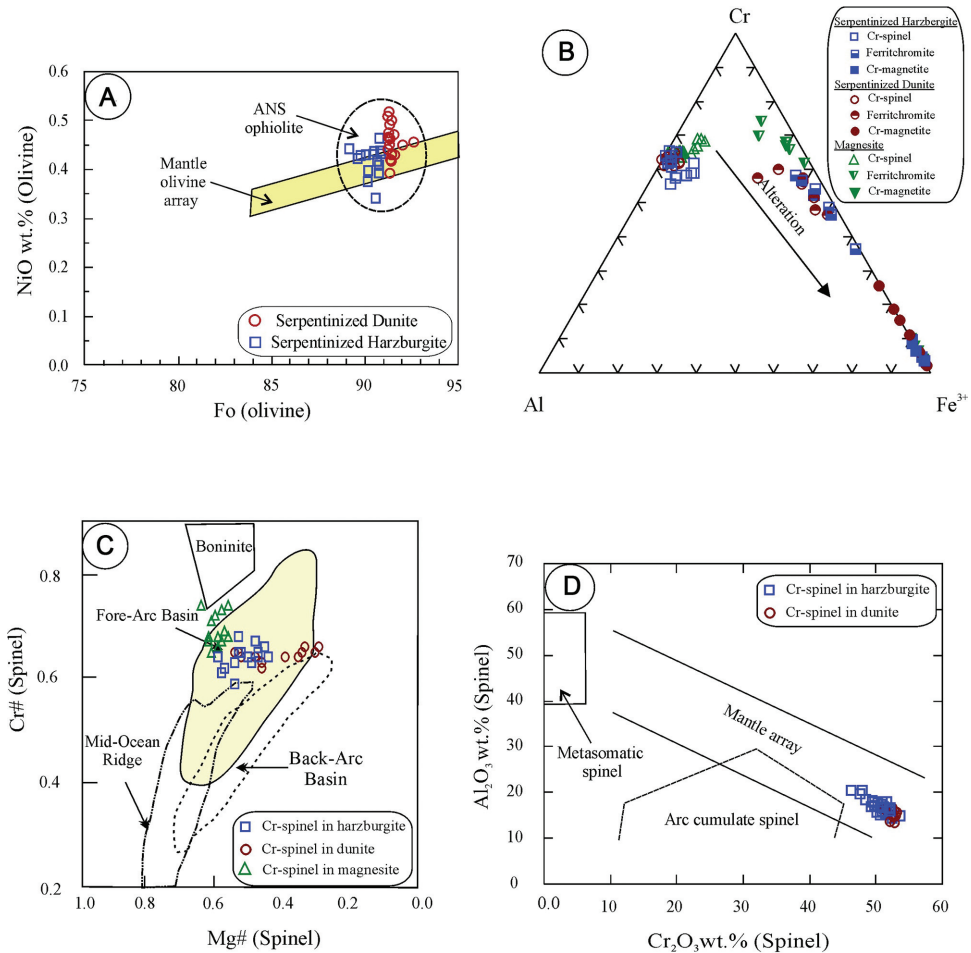
Fig. 6. Mineral chemistry indicators. (A) NiO vs. Fo content of olivine in serpentinized harzburgite and dunite compared to mantle olivine array after Takahashi and others (1987) and field of ANS ophiolites after Khalil and others (2014), Gahlan and others, (2015, 2018), Obeid and others (2016) and Azer and others (2019). (B) Cr–Al–Fe^{3+} plot of chromian spinels and their alteration products. (C) Cr# vs. Mg# diagram for fresh Cr-spinels (after Stern and others, 2004), The melting trend of experimental equilibrium (melting %) is from Hirose and Kawamoto (1995). (D) Cr_2O_3 vs. Al_2O_3 diagram for fresh relics of Cr-spinel (after Franz and Wirth, 2000).

serpentinites in the Eastern Desert of Egypt (for example, Azer, 2014; Khalil and others, 2014; Gahlan and others, 2015).

Cr-spinel in magnesite masses is notably higher in Cr_2O_3 (51.89–54.56 wt.%) and MgO (11.97–13.46 wt.%) than disseminated Cr-spinels in either serpentinized harz-burgite or dunite (44.33–52.32 wt.% Cr_2O_3 and 6.04–12.42 wt.% MgO). Likewise, ferritchromite in magnesite masses is higher in MgO (4.02–7.11 wt.%) and Cr_2O_3 (42.31–51.51 wt.%) and lower in FeO^T (36.58–46.432 wt.%) and MnO (0.63–1.18 wt.%). wt%) than that in the serpentinites (0.67–3.98 wt.% MgO, 24.63–43.06 wt.% Cr_2O_3, 46.56–69.25 wt.% FeO^T and 1.29–1.72 wt.% MnO). Minor silica contents are detected in ferritchromite (0.11–0.29 wt.%) analyses in serpentinite; the spatial pattern of these measurements is inconsistent with secondary fluorescence artifacts, rather they are attributed to effects of alteration (Burkhard, 1993).

The Cr# [molar Cr/(Cr+Al)] of fresh Cr-spinel in serpentinized harzburgite and in dunite are similar, though more scattered in harzburgite (0.59–0.68; av. 0.64 in harzburgite and 0.62–0.66; av. 0.64 in dunite). The Mg# [Molar Mg/(Mg+Fe^{2+})] of fresh Cr-spinel ranges from 0.46 to 0.60 in harzburgite and from 0.30 to 0.55 in dunite. The Cr# and Mg# values are mostly consistent with spinel from peridotites that have been assigned to fore-arc settings in the ANS and elsewhere (for example, Stern and others, 2004; Azer and Stern, 2007; Khalil and others, 2014; Obeid and others, 2016; Gahlan and others, 2018). On the other hand, Cr-spinel in magnesite masses forms a clearly distinct population with higher Cr# (0.65–0.74; av.0.69) and Mg# (0.57–0.65; av. 0.61) (fig. 6C). The Cr_2O_3 and Al_2O_3 contents of fresh Cr-spinel cores of serpentinized harzburgite and dunite plot within the spinel mantle array (Franz and Wirth, 2000) (fig. 6D). The high Cr# (0.59–0.68) and low TiO_2 content (≤ 0.4 wt. %) of spinel indicate that the ultramafic rocks of the Al-Wask ophiolite are depleted residues after high degrees of partial melting (for example, Uysal and others, 2012).

Serpentine Minerals

Chemical compositions and structural formulae (on a 5 O basis) of serpentine minerals are presented in Appendix table A6 and supplementary table 6S. The serpentine minerals are chemically homogeneous and occupy a small range of composition space. They contain 43.09–44.57 wt.% SiO_2, 37.2–41.1 wt% MgO, 0.01–0.56 wt.% Al_2O_3, 1.63–4.99 wt.% FeO, and 0.01–0.21 wt.% Cr_2O_3. Although all the serpentine analyses are similar, there is a statistically significant difference between lizardite (sample W12, Si atoms per formula unit = 2.051 ± 0.018, n = 9) and antigorite (sample W57, Si atoms per formula unit = 2.058 ± 0.014, n = 10).

Amphiboles

The chemical compositions and structural formulae of amphiboles are listed in Appendix table A7 and in supplementary table 7S. The chemical formulae of amphiboles were calculated on the basis of 23 oxygen atoms in the anhydrous total using the 13-CNK method of Leake and others (1997, 2004). The studied amphiboles have low contents of Al_2O_3 (0.80–2.34 wt. %), TiO_2 (0.02–0.11), Na_2O (0.33–0.79 wt. %) and Cr_2O_3 (0.05–0.31 wt. %). The low-TiO_2 contents (≤ 0.11 wt. %) indicate their secondary origin (Girardeau and Mevel, 1982). All the amphibole analyses are calcic and are classified as tremolite according to the nomenclature of Leake and others (1997) (table A7).

Chlorite

The chemical compositions and structural formulae of chlorites are presented in Appendix table A8 and supplementary table 8S. The analyzed chlorites display wide chemical variations in SiO_2, Al_2O_3, Cr_2O_3 and FeO. Few of the chlorite analyses in serpentinized harzburgite are Cr-bearing chlorite (kämmererite; 2.48–3.67 wt. % Cr_2O_3). Using the classification diagram of Hey (1954), the analyzed chlorites are classified mainly as ripidolite and pycnochlorite with minor clinochlore (table A8).

The chemical composition of chlorite can be used to determine the temperature of its formation because its composition is sensitive to prevailing physicochemical conditions during its formation (for example, Kranidiotis and MacLean, 1987; Cathelineau and Nieva, 1985; Cathelineau, 1988; Bourdelle and Cathelineau, 2015; Yavuz and others, 2015). According to the calibrated geothermometer equation of Kranidiotis and MacLean (1987) for chlorite that coexists with aluminous spinel or muscovite, the estimated temperatures for chlorite formation range between 235 and 360 °C, with an average of 286 °C (table 8S).

GEOCHEMICAL CHARACTERISTICS

Based on petrographic examination, 21 serpentinized ultramafic samples showing minimal effects of (late) alteration and weathering (16 harzburgite and 5 dunite) and 12 magnesite samples (7 veins and 5 massive magnesite) were selected for whole-rock XRF analyses at the GeoAnalytical Lab, Washington State University, USA. The samples were crushed to pebble size and then homogenized and pulverized in an agate grinding bowl. Concentrations of major and trace elements were determined on a Ther-moARL X-ray Fluorescence Spectrometer. The complete XRF procedure and its analytical precision and detection limits are listed on the laboratory website (https://environment.wsu.edu/facilities/geoanalytical-lab). Based on the duplicate analyses of samples, the analytical precision is better than 1 percent (2σ) for most major elements, and better than 5 percent (2σ) for most trace elements (except V, Cr, Ni and Sc).

All the serpentinized ultramafic samples (table 1) show high concentrations of MgO (37.34–43.27 wt. %), and moderate total iron as Fe_2O_3 (6.9–8.07 wt. %). Al_2O_3 and CaO contents are usually low (0.35 to 0.92 wt. % Al_2O_3 and 0.34 to 0.79 wt. % CaO). The low and restricted range of CaO and Al_2O_3 contents samples suggest that Ca-metasomatism has had no effect in the Al-Wask serpentinites, despite their proximity to carbonate-altered magnesite and listvenite. All the nalysed samples have high LOI values (11.52–14.29 wt. %), attributable to H_2O in serpentine and CO_2 in carbonate minerals.

Due to the severely serpentinized nature of the ultramafic rocks, the modal percentages of primary minerals cannot be accurately determined and rock classification by a modal scheme such as Streckeisen (1976) can only be approximate. Neglecting changes to anhydrous composition during hydration, however, we can apply a classification based on normative composition (table 2), which places all the serpentinized ultramafic samples in the harzburgite and dunite fields (fig. 7), in agreement with petrographic and field assessments.

All whole-rock Mg# values are high, from 89 to 93, as expected from the mineral chemistry analyses. The range of Mg# is consistent with modern oceanic peridotites (Mg# > 0.89, Bonatti and Michael, 1989) and similar to other ophiolitic serpentinites in the ANS (for example, Azer and others, 2013; Khalil and others, 2014; Obeid and others, 2016; Gahlan and others, 2018). The trace element contents of the ultramafic rocks are highly variable (table 1), but they are uniformly depleted in most trace elements, with the exceptions of the compatible elements Cr (1177–2974 ppm), Ni (1508–2568 ppm), and Co (90–119 ppm). Y, a proxy for heavy rare-earth elements that can be measured by XRF, is <0.4 ppm in all serpentinized peridotite samples.

Whole rock geochemical data for 12 magnesite samples (6 veins and 6 massive magnesite) are shown in table 3. The compositions are surprisingly variable for such nearly monomineralic rocks. The massive-type magnesite has higher SiO_2 (1.65–4.58 wt. %), Fe_2O_3 (0.91–1.24 wt. %), Cr (123–209 ppm), Ni (118–215 ppm), Sr (98–135 ppm), Ba (18–25 ppm), Cu (3–5 ppm) and Pb (15–23 ppm) than the vein-type magnesite. Increased concentration of these particular elements is consistent with an admixture of minor fractions of serpentine minerals, Cr-spinel, calcite, dolomite and magnetite in the massive-type magnesite, as observed petrographically. Disseminated Cr-spinel hosts the elevated Cr content of the massive-type magnesite.

DISCUSSION

Ophiolitic peridotites can be used as petrogenetic indicators for processes that took place in the mantle during formation of the overlying oceanic crust, once due caution is exercised to account for later effects such as serpentinization. Given the long-lived debates about the tectonic history of the ophiolitic rocks of the AS (for example, Bakor and others, 1976; Ledru and Augé, 1984; Nassief and others, 1984; Pallister and others, 1988; Ahmed

TABLE 1

Major and trace element contents in the serpentinized harzburgite and dunite of the Al-Wask ophiolite

Rock type	Harzburgite																Dunite				
Sample	W-1	W-12	W-20	W-24	W-29	W-32	W-35	W-37	W-42	W-44	W-49	W-52	W-57	W-59	W-6	W-9	W-17	W-26	W-40	W-47	W-54
SiO_2	40.42	40.34	37.63	39.34	40.3	39.16	38.49	40.71	39.45	40.44	40.22	38.56	40.38	38.39	37.71	37.76	36.95	35.94	35.96	36.28	36.62
TiO_2	0.02	0.01	0.02	0.03	0.03	0.02	0.02	0.02	0.02	0.02	0.02	0.03	0.02	0.02	0.02	0.03	0.03	0.04	0.02	0.05	0.03
Al_2O_3	0.53	0.35	0.35	0.57	0.38	0.6	0.59	0.38	0.53	0.55	0.43	0.5	0.44	0.58	0.37	0.37	0.53	0.87	0.53	0.92	0.51
Fe_2O_3	7.21	7.26	7.28	7.14	7.23	7.61	7.55	8.67	7.29	7.56	6.9	7.35	7.24	7.49	7.23	7.21	6.72	7.69	7.61	6.47	6.64
MnO	0.07	0.08	0.06	0.07	0.07	0.08	0.06	0.09	0.08	0.08	0.07	0.08	0.07	0.08	0.05	0.08	0.1	0.12	0.12	0.13	0.11
MgO	38.09	38.14	39.46	39.08	37.86	38.32	38.81	36.81	38.91	37.49	38.22	38.98	38.12	38.37	39.83	39.36	41.52	42.75	42.91	43.67	41.91
CaO	0.5	0.41	0.79	0.55	0.34	0.61	0.69	0.4	0.5	0.36	0.47	0.53	0.46	0.68	0.59	0.72	0.55	0.53	0.53	0.55	0.47
Na_2O	0.01	0.02	0.06	0.02	0.01	0.02	0.02	0	0.02	0.02	0.02	0.03	0.02	0.02	0.02	0.06	0.02	0.02	0.02	0.02	0.02
K_2O	0.02	0.01	0.02	0.01	0.02	0.01	0.02	0.01	0.01	0.01	0.01	0.02	0.02	0.01	0.02	0.02	0.02		0.01	0.02	0.02
P_2O_5	0.03	0.02	0.03	0.02	0.02	0.03	0.03	0.03	0.02	0.03	0.03	0.04	0.03	0.03	0.03	0.03	0.01	0.02	0.01	0.02	0.03
LOI	13.01	13.15	14.17	12.98	13.32	13.27	13.78	12.53	13.03	13.11	13.44	13.76	13.08	14	14.29	14.16	13.36	11.63	11.57	11.52	13.44
Total	99.91	99.79	99.87	99.81	99.58	99.73	100.06	99.65	99.86	99.67	99.83	99.88	99.88	99.67	100.16	99.8	99.81	99.61	99.29	99.65	99.8
Mg#	91.28	91.23	91.48	91.56	91.21	90.89	91.06	89.37	91.36	90.76	91.65	91.31	91.25	91.03	91.61	91.54	92.45	91.68	91.78	93.04	92.60
MgO/SiO_2	0.94	0.95	1.05	0.99	0.94	0.98	1.01	0.90	0.99	0.93	0.95	1.01	0.94	1.00	1.06	1.04	1.12	1.19	1.19	1.20	1.14
Al_2O_3/SiO_2	0.01	0.01	0.01	0.01	0.01	0.02	0.02	0.01	0.01	0.01	0.01	0.01	0.01	0.02	0.01	0.01	0.01	0.02	0.01	0.03	0.01
As	4.4	2.3	10	3.9	4.9	4.1	12.3	6.1	4	8.5	6.7	2.8	3.4	5.2	16.3	2.6	13.2	9.9	11	11	4.1
Ba	3	2.2	2.5	26.1	3.5	4.3	18.1	4.2	14.7	4.7	3.3	3.6	2.7	28.5	1.9	3	2.8	2	2	2	1.8
Be	0	0	0	0.1	0	0.3	0.2	0	0.2	0	0	0.2	0	0	0	0	1.4	4.7	4.8	4.5	1.2
Bi	0	0.1	0	0.1	0.1	0	0	0	0	0	0	0	0	0	0	0	0.1	0.2	0.2	0.2	0.1
Co	93	99	112	104	90	106	109	104	106	99	99	102	96	112	106	108	113	118	118	119	110
Cr	1332	1177	1406	1526	1235	1347	1447	1205	1426	1263	1336	1280	1255	1316	1404	1311	1847	2894	2843	2974	1714
Cs	0	0	0	0.1	0.1	0	0.1	0	0	0.1	0	0	0	0.1	0	0	0.3	0.8	0.8	0.8	0.3
Cu	4.9	4.2	3.9	7	3.5	5	6.8	5.6	5.9	3.8	3.4	4	4.5	7.3	0	3.7	4.9	6.1	6	6.1	4.7
Ga	0.7	0.5	5.4	0.7	0.9	0.6	6.7	0.6	0.6	0.9	0.7	0.5	0.6	0.8	10.4	0.4	0.8	1.6	1.7	1.5	0.7
Hf	0	0	0	0	0	0	0	0	0	0	0	0	0	0	0	0	0	0.1	0.1	0.1	0
Li	2.2	0.9	0.5	0.3	4.1	1	1.1	1.1	0.3	2.7	1.1	1.3	1.5	1.3	0.9	0.8	1.7	3.6	3.4	3.8	1.7
Nb	0.1	0	0	0	0.1	0	0	0.1	0	0.1	0.1	0	0	0	0	0	0.1	0.3	0.3	0.3	0.1
Ni	2105	2174	2467	2390	2031	2432	2472	2093	2442	2031	2133	2307	2140	2568	2344	2386	2071	1920	2348	1641	1508
Pb	0.1	0.1	0.1	0.1	0.1	0.1	0.1	0.1	0.1	0.2	0.3	0.1	0.1	0.2	0.1	0.1	0.2	0.4	0.4	0.4	0.2

TABLE 1
(continued)

Rock type	Harzburgite																Dunite				
Sample	W-1	W-12	W-20	W-24	W-29	W-32	W-35	W-37	W-42	W-44	W-49	W-52	W-57	W-59	W-6	W-9	W-17	W-26	W-40	W-47	W-54
Rb	0	0	0	0	0.1	0	0	0.1	0	0.1	0	0	0	0	0	0	0.6	1.8	1.7	1.8	0.6
Sb	0.3	0.2	0.4	0.5	0.2	0.6	0.6	0.2	0.6	0.3	0.4	0.9	0.2	0.5	0.3	0.9	0.5	0.4	0.4	0.5	0.5
Sc	6.9	6.2	6.3	6.4	6.8	6	59	6.2	6.3	6	5.8	6.3	6.5	5.9	6.2	6.5	5.8	5.6	5.5	5.7	5.7
Sn	0.1	0	0	0	0	0.1	0.1	0.1	0	0.1	0	0	0	0	0	0	0.6	1.9	1.9	1.9	0.5
Sr	4.7	4.8	6.9	2.6	5.1	7.9	9.9	4.4	3.5	8	9.7	14.1	4.8	11	8.2	12.9	5.7	2.5	2.3	2.6	4.6
W	0.2	0.3	0.3	0.2	0.3	0.4	0.4	0.2	0.3	0.2	0.2	0.3	0.3	0.3	0.3	0.2	1.2	2.9	2.7	3.1	1.2
Y	0.2	0.2	0	0.1	0.4	0.1	0.1	0.3	0.1	0.4	0.2	0.1	0.2	0.1	0	0	0.2	0.5	0.5	0.5	0.2
Zn	41.8	37.7	40	44.5	38.3	43.2	45	47.2	43.4	48.6	47	43.3	39.7	44.4	38.9	42.3	41.9	47.7	46.5	48.7	41.3
Zr	0.2	0.2	0.3	0.7	0.4	0.3	0.5	0.2	0.4	0.4	0.3	0.3	0.2	0.6	0.2	0.3	1	2.7	2.5	2.7	1
V	25.5	19.4	23.8	27.5	25.1	23.6	25.4	21.9	24.7	24.5	23.5	22.4	22.5	23.5	23	23	24.2	32.2	32.5	31.7	23.2

TABLE 2

Normative compositions for the serpentinized harzburgite and dunite of the Al-Wask ophiolite

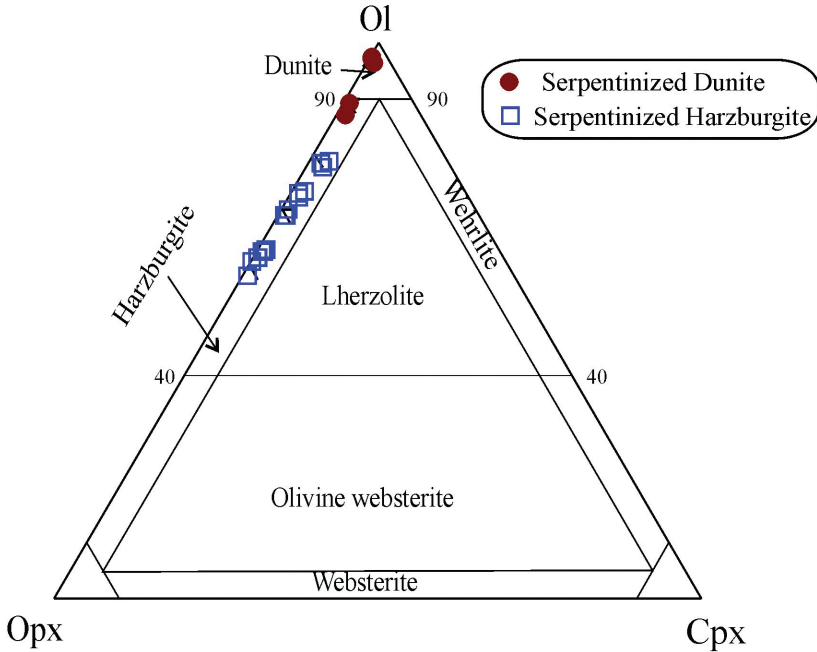| Rock type	Harzburgite																	Dunite			
Sample No.	W-1	W-12	W-20	W-24	W-29	W-32	W-35	W-37	W-42	W-44	W-49	W-52	W-57	W-59	W-6	W-9	W-17	W-26	W-40	W-47	W-54
Orthoclase	0.14	0.07	0.14	0.07	0.14	0.07	0.14	0.07	0.07	0.07	0.07	0.14	0.14	0.07	0.14	0.14	0.14	-	0.07	0.13	0.14
Albite	0.1	0.2	0.6	0.2	0.1	0.2	0.2	-	0.2	0.2	0.2	0.3	0.2	0.2	0.2	0.6	0.2	0.19	0.19	0.19	0.2
Anorthite	1.55	0.97	0.74	1.66	1.09	1.77	1.71	1.17	1.54	1.61	1.23	1.37	1.22	1.72	1.01	0.8	1.51	2.61	1.52	2.7	1.45
Diopside	0.86	0.97	2.85	1.06	0.57	1.2	1.62	0.71	0.93	0.19	0.99	1.1	0.94	1.58	1.72	2.49	1.25	0.19	1.11	0.21	0.82
Hypersthene	35.1	35.28	17.56	27.51	36.68	28.31	23.7	39.6	28.62	37.53	34.68	24.72	35.01	25.04	18.92	18.89	11.21	2.53	2.37	2.1	9.54
Olivine	59.88	60.16	75.68	67.14	59.03	65.96	70.16	55.72	66.27	57.94	60.53	69.88	60.11	68.9	75.6	74.65	83.44	91.94	92.28	92.4	85.55
Magnetite	1.84	1.86	1.88	1.83	1.86	1.96	1.94	2.21	1.87	1.94	1.77	1.9	1.85	1.94	1.86	1.87	1.74	1.96	1.94	1.65	1.72
Ilmenite	0.04	0.02	0.04	0.07	0.07	0.04	0.04	0.04	0.04	0.04	0.04	0.07	0.04	0.04	0.04	0.07	0.07	0.09	0.04	0.11	0.07
Apatite	0.08	0.05	0.08	0.05	0.05	0.08	0.08	0.08	0.05	0.08	0.08	0.1	0.08	0.08	0.08	0.08	0.03	0.05	0.03	0.05	0.08
Color Index	97.72	98.3	98.02	97.6	98.21	97.48	97.46	98.29	97.73	97.64	98.01	97.67	97.96	97.52	98.15	97.96	97.69	96.7	97.75	96.48	97.7
Diff. Index	0.24	0.27	0.74	0.26	0.24	0.27	0.34	0.07	0.26	0.27	0.27	0.44	0.33	0.27	0.34	0.74	0.33	0.19	0.26	0.33	0.33

Fig. 7. Nomenclature of Jabal Al-Wask serpentinized ultramafic rocks based on Ol-Opx-Cpx normative composition, compared to field and petrographic assignment (after Coleman, 1977).

and Hariri, 2008; Ahmed and Habtoor, 2015; Ahmed and Surour, 2016), new contributions that might constrain their interpretation are welcome. In the case of the Al-Wask ophiolite, despite its size and excellent exposure, there have been few detailed field studies and limited mineralogical or petrological data. Therefore, we attempt to combine our observations from field study, petrography, mineralogy and geochemistry to deduce the tectonic setting of the ultramafic sequence and hence of the whole ophiolite and then to place it in the broader context of the Neoproterozoic evolution of the AS.

Metamorphism

Clearly, the ultramafic rocks of the Al-Wask ophiolite have undergone various degrees of deformation, metamorphism and alteration. This is shown by the petrographic abundance of alteration minerals, dearth of primary minerals, and the high LOI. The observed mineral assemblage in some of the ultramafic samples (antigorite–magnetite–tremolite–chlorite±talc, with residual olivine and Cr-spinel) is consistent with upper greenschist to lower amphibolite facies metamorphism (for example, Evans and Trommsdorff, 1974; Evans, 1977). Petrographic observation, X-ray diffraction, and Raman spectroscopy indicate that the main serpentine mineral in ultramafic samples such as W57 is antigorite, with minor chrysotile in distinct veins. Generally, antigorite is the high-temperature polytype of serpentine, stable at higher temperatures than chrysotile and lizardite (Falk and Kelemen, 2015); the boundary temperature depends on pressure, silica activity, water activity, and iron content but it remains generally near 200 °C. In the present case, the abundant antigorite in these samples is interpreted to represent hydration of primary mafic mineral phases (for example, Evans, 1977; Deer and others, 1992; Azer and Khalil, 2005; Derbyshire and others,

Major and trace element concentrations in the magnesite deposits of the Al-Wask ophiolite

	Magnesite veins						Massive magnesite					
	VM2	VM6	VM9	VM12	VM15	VM18	MM1	MM4	MM7	MM10	MM13	MM15
SiO_2	1.21	1.04	0.72	1.31	0.91	0.65	1.65	3.61	4.58	3.32	3.27	2.08
TiO_2	0	0.01	0.02	0	0	0.01	0.01	0.02	0.03	0.05	0.05	0.06
Al_2O_3	0.08	0.01	0.42	0.02	0.15	0.03	0.25	0.39	0.49	0.51	0.37	0.69
Fe_2O_3	0.18	0.1	0.24	0.21	0.32	0.19	1.06	0.91	1.24	0.97	1.15	1.07
MnO	0.01	0.01	0.03	0.02	0.06	0.02	0.02	0.04	0.07	0.04	0.04	0.04
MgO	42.72	42.65	41.45	41.48	43.39	43.08	41.19	39.74	39.1	40.45	40.14	40.01
CaO	4.31	4.57	5.12	5.14	2.99	3.62	2.38	3.01	4.91	3.04	3.64	4.09
Na_2O	0	0.04	0.01	0.03	0	0	0.01	0.02	0.03	0.02	0.03	0.01
K_2O	0.01	0	0.04	0.03	0.01	0.02	0.02	0.01	0.02	0.03	0.02	0.01
P_2O_5	0.02	0.11	0.09	0.03	0.04	0.02	0.11	0.07	0.06	0.04	0.08	0.15
LOI	51.01	51.12	51.1	50.93	50.65	52.02	52.95	51.12	49.29	51.42	50.8	51.17
Total	99.55	99.66	99.24	99.2	98.52	99.66	99.65	98.94	99.82	99.89	99.59	99.38
Ni	4.6	3.5	8.4	4.7	9.6	8.4	118.3	156.1	214	206.6	168.5	215.3
Cr	6.3	11.6	6.4	4.9	4.6	5.3	167.3	122.6	158.4	188.6	209	161.6
Sc	1.2	0.6	1.1	0.5	2.1	1.2	1.2	1.2	1.3	1.26	1.4	1.3
V	8.7	8.3	10.8	9.8	12.3	7.3	20.1	20.2	16.7	18.9	17.6	25.6
Ba	4	7.3	14.2	7.1	12.5	8.03	20.3	21.7	18.2	17.6	15.2	24.8
Rb	0.6	0.7	1.8	1.4	1.9	1.1	1.8	1.1	1.5	1.6	1.4	1.7
Sr	81.9	71.2	77.9	75.3	74.1	81.7	97.8	135.4	115.2	120.4	108.6	126.6
Zr	2.3	2.2	3.4	1.7	3.1	1.7	2.2	2.7	4.4	4.1	4.3	2.5
Y	1.4	2.8	3.7	0.8	5.6	2.5	1.3	1.8	1.4	1.3	1.2	1.5
Ga	1.3	0.5	1.7	0.7	1.3	0.6	0.8	0.9	0.6	0.7	0.8	0.9
Cu	1.8	3.5	2.1	2.8	6.7	4.3	3.6	4.8	2.9	3.7	3.9	3.8
Zn	5.8	7.1	7	6.2	12.1	9.8	6.4	8.1	5.3	4.9	6.8	5.8
Pb	4.5	4.7	5.3	7.1	5.6	6.2	22.6	14.7	18.6	18.6	20.4	23.1

2013), whereas minor chrysotile in cross-cutting veins indicates a small amount of later, lower temperature recrystallization. The preserved mesh and bastite textures pseudo-morphing primary olivine and orthopyroxene suggest that the antigorite formed directly from primary mafic minerals without an intervening early stage of serpentinization. Antigorite-dominated samples contain only minor carbonate as magnesite and show little evidence of extensive interaction with CO_2-bearing fluids.

Cr-spinels of the Al-Wask ophiolite preserve fresh cores mantled by ferritchromite and rimmed by Cr-magnetite. Ferritchromite formation has been associated with temperatures near 500 °C and upper greenschist or lower amphibolite facies metamorphism (for example, Evans and Frost, 1975; Kimball, 1990; Suita and Streider, 1996; Mellini and others, 2005; Azer and others, 2019).

The presence of kämmererite (Cr-rich chlorite), which derives its Cr content from decomposition of Cr-spinel, reflects a low-temperature episode of alteration. During the alteration of chromian spinel to ferritchromite, most Cr and Fe enter into ferritchromite, whereas Al and Mg are released to the surrounding silicate minerals. Later, at somewhat lower temperatures, the vailable Al supports alteration of serpentine to chlorite and liberation of sufficient Cr to produce kämmererite (Azer and Stern, 2007; Gahlan and others, 2018). The inferred temperatures for the formation of disseminated chlorite and kämmererite range between 235 and 360 °C, with an average of 286 °C. However, the distinct boundaries between Cr-spinel cores and their ferritchromite rims together with the high-Cr spinels preserved in the massive magnesites both indicate that the Cr# of the

spinel cores has not been raised by chlorite formation and can be taken as a minimum for the composition of primary residual spinels after melt extraction.

Some of the serpentinized harzburgites lack antigorite. These samples are modally dominated by lizardite and disseminated magnesite, as shown by X-ray diffraction, Raman spectroscopy, and optical examination. In principle, it is possible that the lizardite-dominated samples experienced lower peak metamorphic conditions than the antigorite-dominated samples, or they may have recrystallized from earlier antigorite upon cooling. Likewise, in principle the antigorite-dominated samples may have been initially serpentinized in the stability field of lizardite and then been recrystallized at higher temperature or they may have formed antigorite directly from igneous precursor minerals. We argued above that the preservation of mesh and bastite textures in the antigorite serpentinite suggests direct formation of antigorite from olivine and orthopyroxene. Furthermore, the presence of abundant magnesite specifically in the lizardite-bearing samples offers an additional clue.

Boskabadi and others (2017) describe an occurrence in the Meatiq Dome area of the Central Eastern Desert of Egypt where lizardite and antigorite serpentinites are found in geographically distinct parts of a single massif. In the Meatiq case, the lizardite-rich specimens preserve mesh texture, whereas the antigorite-rich specimens have no remaining pseudomorphs after primary igneous minerals and are also heavily converted to magnesite. These authors conclude that the lizardite-forming process was the initial serpentinization stage and that antigorite serpentinites are recrystallized from lizardite serpentinite. The current case at Al-Wask is different; it is the antigorite that preserves mesh texture and the lizardite that coexists with abundant disseminated magnesite.

Lizardite and magnesite together is an unusual mineral assemblage. To determine its stability field and test whether these samples might represent equilibrium assemblages at some conditions, we carried out thermodynamic calculations with Perple_X (Connolly, 2005) in the chemical system $MgO-SiO_2-H_2O-CO_2$. All calculations used Perplex_X version 6.8.7, the Holland and Powell (2011) mineral database version 6.3.3, and the H_2O-CO_2 fluid equation of state with Pitzer and Sterner (1994) end-member properties and mixing terms from Holland and Powell (2003). The results are shown in figure 8. Figure 8A shows that fluid-saturated peridotite bulk compositions have a significant stability field for antigorite+magnesite, but not for lizardite+magnesite. The topologies of these fields are different in Perple_X because of the small but significant difference in stoichiometry that Perple_X assumes for lizardite ($Mg_3Si_2O_5(OH)_4$) and antigorite ($Mg_{48}Si_{34}O_{85}(OH)_{62}$). The increase in silica activity promoted by carbonation thus favors antigorite over lizardite, when the variance allows. Essentially, with decreasing temperature at constant pressure, the magnesite-in boundary sweeps across from pure CO_2 at 800 K to essentially pure H_2O at 300 K. At temperatures low enough to form lizardite rather than antigorite (<460 K at 2000 bars), quartz+magnesite is stable relative to lizardite+brucite if the fluid contains any appreciable CO_2 at all. Logarithmic activity diagrams provide an alternative way of viewing the very low-CO_2 part of the system; figures 8B and 8C reveal that there is a boundary at specific values of SiO_2 activity, CO_2 activity, temperature, and pressure where lizardite coexists with magnesite. For appropriate values of SiO_2 activity, cooling through the antigorite field at constant CO_2 activity will eventually cause magnesite saturation. If the volume of fluid is limited enough that the system is rock-buffered rather than fluid-buffered, the formation of magnesite will draw down the CO_2 activity, allowing the system to track along the antigorite+magnesite boundary until (for the particular pressure and SiO_2 activity shown), lizardite begins to form at 338 K. Continued addition of fluid could then continue to generate more magnesite, leading to preservation of a lizardite+magnesite rock. The capacity of the fluid to
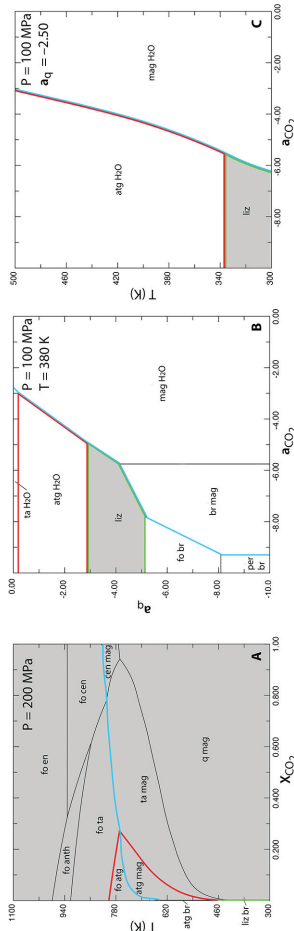
Fig. 8. Perple_X calculations of mineral stability in the MgO-SiO$_2$-H$_2$O-CO$_2$ system. (A) Fluid-saturated surface at molar MgO/SiO$_2$ = 1.07 and pressure 2000 bars, plotted in temperature vs. mole fraction CO$_2$ in the fluid phase. Mineral abbreviations: fo (forsterite), en (orthoenstatite), cen (clinoenstatite), anth (anthophyllite), ta (talc), atg (antigorite), mag (magnesite), br (brucite), liz (lizardite), q (quartz). The stability field of antigorite is outlined in red, of lizardite in green, and of magnesite in blue. Note there is a substantial combined field for antigorite+magnesite, extending upwards from 460 K. However, there is no field for lizardite+magnesite, and lizardite is compressed to the extreme left-hand side of the diagram where it coexists with nearly pure H$_2$O fluid. The same general relations hold for MgO/SiO$_2$ ratios from 1.0 to 2.2 (not shown). (B) A plot of stability fields in activity-activity space, log$_{10}$(a$_{SiO2}$) vs. log$_{10}$(a$_{CO2}$), constructed at 1000 bars, 380 K, and with molar MgO/H$_2$O = 1.5. a_q is SiO$_2$ activity referenced to quartz at unit activity; a$_{CO2}$ is referenced to pure CO$_2$ vapor at unit activity. The limits of lizardite, antigorite, and magnesite are outlined in color as before. This plot reveals that lizardite can coexist with magnesite+vapor along a specific reaction boundary at this temperature near log$_{10}$(a$_{CO2}$) = −5. At this temperature, lizardite exposed to a finite quantity of CO$_2$-bearing fluid will react to form magnesite, consuming CO$_2$ and liberating SiO$_2$ until the fluid activities reach a boundary of the lizardite field. (C) This section is drawn at fixed SiO$_2$ activity 2.5 log units below quartz saturation and at 1000 bars pressure, with the independent axes being temperature and log$_{10}$(a$_{CO2}$). This maps out scenario for formation of lizardite+magnesite rocks upon cooling of antigorite serpentinites. Cooling at any fixed CO$_2$ activity will lead to magnesite saturation, driving the system along the boundary between the antigorite+H$_2$O and magnesite+H$_2$O fields until 338 K, where lizardite can form. Continued cooling will force the activity of CO$_2$ ever lower, precipitating increasing amount of magnesite.

remove aqueous SiO_2 from the system will affect the detailed path of SiO_2 activity and hence the temperature at which lizardite forms.

This scenario is most consistent with metamorphism of the entire massif to at least upper greenschist facies, converting olivine and orthopyroxene in the whole ultramafic section almost quantitatively to antigorite. CO_2 content of the serpentinizing fluid was low (mole fraction ≤ 0.3). Upon cooling from peak metamorphic conditions, some areas of the massif preserved the antigorite-dominated lithology, perhaps due to low fluid activity, low strain, or rapid decompression. Other areas became saturated with magnesite, driving the CO_2 activity in the fluid down along the antigorite+magnesite boundary until, at sufficiently low temperature, antigorite was converted to lizardite. The serpentine textures, relative abundance of magnesite in different lithologies, and petrological modelling lead us to a different interpretation than that proposed by Boskabadi and others (2017) for the Meatiq Dome example.

Tectonic Setting

The AS ophiolites are important elements for reconstructing the geodynamic evolution of the ANS Pan-African belt. However, ophiolites can originate in diverse and complex tectonic settings, fingerprints of which can be found in their whole-rock and mineral chemistry. The AS ophiolites have in fact been assigned to a range of inconsistent tectonic settings. Petrological studies have been interpreted to indicate formation in both mid-ocean ridge (MOR) and supra-subduction zone (SSZ) settings (for example, Neary and Brown, 1979; Quick, 1990; Ahmed and others, 2012; Ahmed and Habtoor, 2015; Ahmed and Surour, 2016; Habtoor and others, 2017). The debate about tectonic setting of AS ophiolites in general is mirrored in work on the Al-Wask ophiolite in particular (Bakor and others, 1976; Kemp, 1981; Ledru and Augé, 1984). Bakor and others (1976) interpreted the Al-Wask ophiolite complex as a back-arc ophiolite, while Kemp (1981) regarded the complex as a non-ophiolitic intrusion altogether. Ledru and Augé (1984) rejected emplacement of the sequence by obduction on a low-angle fault and treated the Al-Wask ophiolite as a mafic-ultramafic assemblage emplaced by vertical movement along a subvertical shear zone.

The present study indicates that the serpentinized ultramafic rocks of the Al-Wask ophiolite are derived mainly from harzburgite with minor dunite, similar in this regard to the ultramafic tectonites formed in supra-subduction environments (for example, Pearce and others, 1984; Qiu and others, 2007). The Al-Wask ophiolite ultramafic rocks have MgO/SiO_2 (0.90–1.20) and Al_2O_3/SiO_2 (0.01–0.03) ratios similar to fore-arc peridotites (fig. 9A) (Parkinson and Pearce, 1998; Pearce and others, 2000; Niu, 2004). On the MgO/SiO_2 versus Al_2O_3/SiO_2 diagram (Jagoutz and others, 1979; Hart and Zindler, 1986), the samples plot at low Al_2O_3/SiO_2 (fig. 9A); the harzburgites in particular resemble residues of a mantle source that experienced high degrees of partial melt extraction, higher than is typical of MOR settings. The serpentinized peridotite samples from the Al-Wask ophiolite containing no carbonates are depleted in Al_2O_3 and CaO, similar to typical fore-arc peridotites (fig. 9B). Likewise, all the ultramafic samples have low TiO_2 (≤ 0.05 wt. %), which is characteristic of arc-related peridotites that experienced high degrees of partial melt extraction (for example, Arai, 1992; Kamenetsky and others, 2001; Uysal and others, 2012).

The chemistry of relict primary minerals, particularly olivine and spinel, are often used to infer tectonic settings, even in highly serpentinized ultramafic rocks (for example, Azer and Stern 2007; Khalil and others, 2014; Obeid and others, 2016; Gahlan and others, 2018; Azer and others, 2019, among others). Indeed, the mineral chemistry characteristics of primary phases in the Al-Wask serpentinites support a fore-arc tectonic setting. This is compatible with recent studies of the tectonic settings of rocks of similar age throughout the ANS (for example, Azer and others, 2013; Khedr
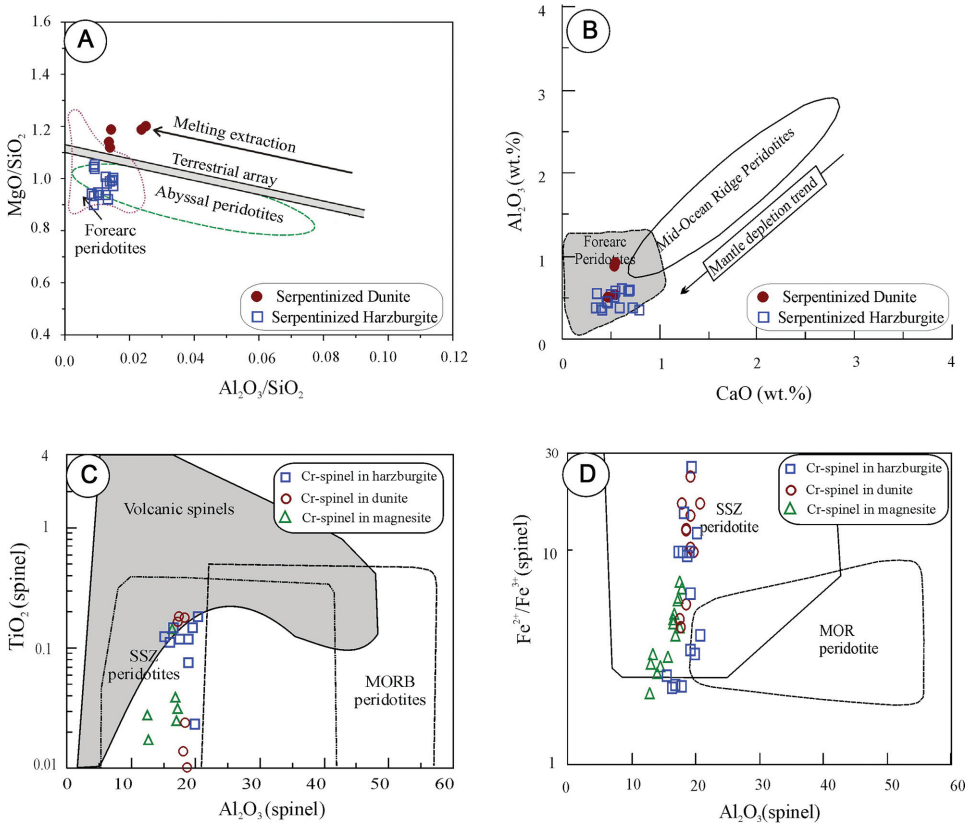
Figure 9. (A) MgO/SiO$_2$ versus Al$_2$O$_3$/SiO$_2$ diagram comparing Jabal Al-Wask ultramafic rocks to the abyssal peridotite field after Niu (2004), the field of fore-arc peridotites after Pearce and others (2000) and Parkinson and Pearce (1998), and the terrestrial array after Jagoutz and others (1979) and Hart and Zindler (1986). (B) Al$_2$O$_3$ versus CaO diagram for serpentinized ultramafic rocks of Jabal Al-Wask compared to fields of Ishii and others (1992). (C) TiO$_2$ versus Al$_2$O$_3$ discrimination diagram of chromian spinel (after Kamenetsky and others, 2001). (D) Al$_2$O$_3$ vs. Fe^{2+}/Fe^{3+} diagram for spinels showing the fields of supra-subduction zone (SSZ) and mid-ocean ridge (MOR) peridotite (after Kamenetsky and others, 2001).

and Arai, 2013; Azer, 2014; Gahlan and others, 2015). On the Al$_2$O$_3$ vs. TiO$_2$ and Al$_2$O$_3$ vs. Fe^{2+}/Fe^{3+} diagrams (Kamenetsky and others, 2001), the compositions of primary Cr-spinels from Al-Wask lie squarely in the SSZ peridotite field (figs. 9C and 9D) and their Cr# (mostly >0.60) is similar to those of modern fore-arc peridotites (fig. 6C). The forsterite and NiO-rich nature of fresh olivine from the Al-Wask serpentinites is also consistent with residual mantle olivine from rocks that experienced extensive melting, as in fore-arc peridotites (for example, Arai, 1994; Pearce and others, 2000; Coish and Gardner, 2004). Degrees of partial melting, estimated based on the Cr# of fresh spinel cores and interpreted here as lower limits, are 32 to 38 perhaps (fig. 6C), similar to those of supra-subduction zone peridotites (15–40%; Parkinson and Pearce, 1998; Pearce and others, 2000). The measured concentrations of Y, a moderately incompatible and fluid-immobile element similar in behaviour to the heavy rare-earth elements, also provide a quantitative estimate of the degree of melting. All the serpentinized harzburgites have <0.4 ppm Y (most are ~0.1 ppm Y), which is <0.1x the primitive mantle concentration (0.43 ppm, Sun and McDonough, 1995). Fractional melting models with experimentally constrained

partition coefficients show that such depletion requires ≥25 percent melt extraction (for example, Niu, 2004).

Petrogenesis of Magnesite

Carbonation of ultramafic rocks in the crust and mantle is an important geological process with implications for the formation of ore deposits and for the balance of CO_2 fluxes to and from the Earth's atmosphere (for example, Skelton, 2011; Kelemen and Manning, 2015; Boskabadi and others, 2017). The carbonation occurs when silicate rocks interact with CO_2-bearing fluids, promoting alteration reactions that precipitate carbonates and other minerals, including in some cases talc and gold (Groves and others, 1998; Boskabadi and others, 2017). Mafic and ultramafic rocks are particularly susceptible to carbonation, with significant reaction rates even at relatively low temperatures. Natural and potentially artificial mineral carbonation have drawn attention in the contexts of historical climate changes and the search for means of sequestration of anthropogenic CO_2 emissions in geological reservoirs (for example, Kelemen and others, 2011, 2018; Power and others, 2013).

Reaction between CO_2-bearing fluids and olivine or serpentine usually produces the industrially useful mineral magnesite ($MgCO_3$) (for example, Kelemen and Matter, 2008; Klein and Garrido, 2011), which is commonly found worldwide in networks of veins in the ultramafic parts of ophiolite sequences. A key question concerning the formation of such magnesite is the source of CO_2-bearing fluids, whether they are of hydrothermal (magmatic or metamorphic) or superficial origin (for example, Fallick and others, 1991). Most studies using stable isotopes have concluded that the fluids are dominantly meteoric (for example, Launay and Fontes, 1985; Clark and Fontes, 1990; Fallick and others, 1991; Bruni and others, 2002; Gartzos, 2004; Kelemen and others, 2011; Oskierski and others, 2013; Boskabadi and others, 2017; Canovas and others, 2017; de Obeso and Kelemen, 2018). However, a considerable number of factors affects the stable isotope composition of preserved carbonates, including kinetic and temperature effects as well as source fluid composition (for example, Falk and others, 2016).

In the ANS, most of the known magnesite ores are associated with structural features such as faults and shear zones cutting through serpentinized ophiolitic peridotites. Published literature on the ANS magnesite deposits is sparse and leaves questions of their timing and origin unsettled (for example, Stern and Gwinn, 1990; Boskabadi and others, 2017; Azer and others, 2019). Early work by Stern and Gwinn (1990) suggested a mixed mantle and sedimentary carbon source based on C, O, and Sr isotope ratios, whereas more recent stable studies of stable C, O, and H isotope ratios indicate an exclusively mantle-derived carbon source (for example, Boskabadi and others, 2017; Hamdy and Gamal El Dien, 2017). Other authors have adopted a model of metamorphic degassing as the CO_2 source leading to magnesite veins along tectonic fractures in serpentinite (for example, Shukri and Lutfi, 1959; Salem and others, 1997; Ghoneim and others, 1999, 2003; Hamdy and Lebda, 2007).

A meteoric scenario for magnesite formation, especially one related to weathering upon modern exposure, would not be expected to require a close connection between carbonation and tectonic events or structures. However, there is substantial evidence to the contrary. Some authors have noted close links between carbonated ultramafic rocks and tectonic events (for example, Dabitzias, 1980) and structures (Kelemen and others, 2011; Azer and others, 2019). Recent studies (Quesnel and others, 2013; Borojević Šoštarić and others, 2014; Falk and Kelemen, 2015; Scarsi and other, 2018; Menzel and others, 2018; Azer and others, 2019) demonstrate that magnesite veins formed at the base of some obducted ophiolites during shear deformation, and not at the exposed surface. These examples of syn-tectonic carbonation imply that tectonic events including ophiolite development, near-ridge detachment faulting, and ophio-

lite obduction may be genetically linked and contemporaneous with the suite of alteration processes leading to magnesite veins and the formation of associated ore deposits, at least in some metallogenic provinces.

The present study found clear evidence for two different styles of magnesite occurrence in the Al-Wask ophiolite, namely massive and vein-type magnesite deposits. This is interpreted to reflect at least two successive stages of serpentinite carbonatization, likely with different fluid sources. In the first stage, magnesite masses were formed after leaching of magnesia and other components by CO_2-bearing solutions and deposition of magnesite in the pore space opened by loss of solid volume. Such a replacement mechanism is supported by the presence of Cr-spinel in the massive magnesite, similar in composition to that in the host serpentinite, and the presence of some angular to sub-angular fragments of serpentinite. The formation of magnesite by replacement of serpentinite protoliths requires a substantial input of externally-derived CO_2 in order to achieve nearly complete replacement of the original serpentine minerals (Quesnel and others, 2013; Borojević Šoštarić and others, 2014; Falk and Kelemen, 2015; Scarsi and others, 2018; Menzel and others, 2018). Azer and others (2019) interpreted similar magnesite types as the products of deep-seated metasomatism and alteration, synchronous with serpentinization during the final stages of emplacement of the mantle section into fore-arc oceanic lithosphere. An obvious and abundant source for CO_2-bearing fluids in such an environment is the decomposition of carbonates in the subducted slab underlying the original fore-arc (Quesnel and others, 2013; Borojević Šoštarić and others, 2014; Falk and Kelemen, 2015; Scarsi and other, 2018; Menzel and others, 2018; Azer and others, 2019).

The magnesite veins have a different origin from the massive magnesite. Field relations and petrographic observation show that the magnesite veins formed after serpentinization and fill tectonic fractures that likely represented conduits for ascending or circulating hydrothermal solutions carrying CO_2 and Mg^{2+}. These veins are entirely consistent with widely accepted models of the formation of magnesite veins that involve meteoric fluid circulation and vein precipitation, after obduction of the ophiolite, and limited to depths of a few hundred meters below the current or paleo-exposure surface. Fluids of meteoric origin that infiltrate the sole thrust of an ophiolite and then discharge through the upper plate of a thrust system experience decompression leading to saturation of magnesite, most likely at temperatures below 300 °C (Johannes, 1970). Such an origin is consistent with the following observations: (1) the veins are predominantly cryptocrystalline, mono-mineralic magnesite; (2) no angular fragments of serpentinite host are observed within the magnesite veins; and (3) there are no relics of minerals such as chromian spinel, olivine, orthopyroxene, or serpentine in magnesite veins. The cryptocrystalline texture of magnesite indicates a rapid addition of CO_2-rich fluids and precipitation of magnesite from solutions under near-surface conditions (Azer and others, 2019).

The present study indicates that the Cr-spinel enclosed in the magnesite masses is notably higher in Cr_2O_3 and MgO than disseminated Cr-spinels in either serpentinized harzburgite or dunite. Given the presence of fragments of serpentinite in the massive magnesite, we consider the Cr-spinels in the magnesite to be relics derived from the replaced serpentinized peridotite. Now, given the presence of some Al-bearing amphibole and chlorite phases in the serpentinized peridotite, there is a chance that the Cr# of the primary spinels in peridotite was raised by loss of Al to these metamorphic phases. However, if this had been the case then we would expect to observe the opposite relationship between spinel in serpentinite and in magnesite. That is, the unexchanged spinels in magnesite would preserve an original low-Cr# composition. Once encased in carbonates, spinels become highly resistant to exchange or alteration due to the absence of nearby silicate phases with which to exchange (Gahlan and

others, 2018). Therefore, the spinels captured in massive magnesite early in serpentinization and at high temperature likely reveal a more primary composition than those now found in serpentinite matrix. It is not clear what process might have lowered the Cr# of the spinels in the serpentinites, but the data certainly argue against the idea that there has been significant increase in the Cr# of the serpentinite spinels during metamorphism. Their present Cr# is likely a lower bound on their primary Cr#. This argument lends support to the conclusions drawn above about the refractory character of the peridotite protoliths, the high degrees of melt extraction that they experienced, and their likely assignment to a fore-arc setting.

CONCLUSIONS

1. The Al-Wask ophiolite is a weakly dismembered ophiolite sequence; most lithologies of the classic sequence are present in order, although layered gabbro is highly attenuated and sheeted dikes are missing. The ophiolite has undergone multiple phases of alteration, deformation and metamorphism up to at least greenschist facies. The pervasive shearing during ophiolite emplacement and extensive serpentinization, carbonatization and silicification resulted in the development of magnesite and listvenite along shear zones.

2. All primary silicate minerals in the ultramafic mantle section have been replaced by serpentine minerals, except for a few relics of fresh olivine and chromian spinel. The Al-Wask serpentinized ultramafics display bastite and mesh textures after orthopyroxene and olivine, reflecting exclusively harzburgite and dunite protoliths. The presence of antigorite-dominated serpentinites indicates that (at least parts of) the Al-Wask ultramafic sequence was hydrated at relatively high temperature (Evans, 1977).

3. The serpentinized ultramafics of the Al-Wask ophiolite show low whole-rock SiO_2, TiO_2, CaO, and Al_2O_3 contents combined with high MgO, Mg#, Ni, Co and Cr contents that all point to highly refractory mantle protoliths as commonly found in supra-subduction zone settings, most likely a fore-arc. The high Cr# and low TiO_2 content of fresh spinel relics and the high Fo-contents of associated primary olivine are consistent with this interpretation, indicating residual mantle after extensive melt extraction.

4. Magnesite in the Al-Wask ophiolite forms both massive and vein types. Massive magnesite formed by alteration and replacement of ultramafic rocks with evidence of structural control that localized the CO_2-bearing fluid flux. The massive magnesite generation is correlated with lizardite-dominated serpentine assemblages, suggesting the coexistence of magnesite and lizardite developed upon cooling of antigorite serpentinite at a specific CO_2-buffered reaction boundary. Fluids driving reaction during this cooling stage may have involved CO_2 derived from underlying, subducted carbonates, perhaps during ophiolite emplacement. The vein magnesite, by contrast, formed superficially, after serpentinization and obduction, involving meteoric fluid circulation and precipitation in fractures rather than by replacement of serpentinite.

APPENDIX

TABLE A1

Microprobe analyses of olivines in the serpentinized harzburgite of the Al-Wask ophiolite

| Sample No. | W12 | | | | | | | | | | W57 | | | | |
Mineral	Primary olivine										Primary olivine				
SiO_2	41.235	41.421	41.295	41.025	41.135	41.42	41.247	41.12	40.53	40.422	40.623	41.725	41.016	40.76	40.904
TiO_2	0.006	0.007	0	0	0.023	0.007	0	0.008	0.01	0.006	0.003	0.006	0	0.003	0.004
Al_2O_3	0	0.006	0.008	0	0.009	0.006	0	0.003	0	0.01	0.003	0	0.004	0.005	0
Cr_2O_3	0.003	0.019	0.057	0	0.001	0.034	0.028	0.015	0.015	0.016	0.01	0.021	0.025	0.026	0.006
FeO	8.786	9.27	10.481	9.226	9.736	9.226	8.641	9.766	8.755	8.981	8.728	9.523	8.69	8.936	8.753
MnO	0.145	0.141	0.112	0.116	0.141	0.146	0.113	0.133	0.141	0.116	0.135	0.115	0.135	0.14	0.133
MgO	49.341	49.016	49.506	49.921	48.556	48.726	49.598	49.144	49.711	49.803	49.923	49.601	49.848	49.494	49.603
CaO	0.027	0.023	0.016	0.035	0.029	0.045	0.021	0.028	0.023	0.016	0.066	0.033	0.01	0.044	0.032
NiO	0.411	0.372	0.441	0.424	0.416	0.394	0.426	0.425	0.406	0.337	0.458	0.427	0.433	0.43	0.391
Total	99.954	100.275	101.916	100.747	100.046	100.00	100.074	100.64	99.59	99.707	99.949	101.451	100.161	99.838	99.826
Structural formulae															
Si	1.007	1.009	0.997	0.997	1.008	1.012	1.005	1.002	0.995	0.992	0.994	1.006	1.000	0.998	1.001
Ti	0.000	0.000	0.000	0.000	0.000	0.000	0.000	0.000	0.000	0.000	0.000	0.000	0.000	0.000	0.000
Al	0.000	0.000	0.000	0.000	0.000	0.000	0.000	0.000	0.000	0.000	0.000	0.000	0.000	0.000	0.000
Cr	0.000	0.000	0.001	0.000	0.000	0.001	0.001	0.000	0.000	0.000	0.000	0.000	0.000	0.001	0.000
Fe(ii)	0.179	0.189	0.212	0.187	0.199	0.189	0.176	0.199	0.180	0.184	0.179	0.192	0.177	0.183	0.179
Mn	0.003	0.003	0.002	0.002	0.003	0.003	0.002	0.003	0.003	0.002	0.003	0.002	0.003	0.003	0.003
Mg	1.796	1.781	1.782	1.808	1.773	1.775	1.802	1.785	1.819	1.822	1.821	1.784	1.811	1.808	1.809
Ni	0.008	0.007	0.009	0.008	0.008	0.008	0.008	0.008	0.008	0.007	0.009	0.008	0.008	0.008	0.008
Ca	0.001	0.001	0.000	0.001	0.001	0.001	0.001	0.001	0.001	0.000	0.002	0.001	0.000	0.001	0.001
Endmembers															
Fo	90.78	90.28	89.28	90.50	89.76	90.26	90.99	89.85	90.88	90.71	90.94	90.17	90.97	90.67	90.87
Fa	9.07	9.58	10.60	9.38	10.09	9.59	8.89	10.01	8.98	9.17	8.92	9.71	8.89	9.18	8.99
Tp	0.15	0.15	0.11	0.12	0.15	0.15	0.12	0.14	0.15	0.12	0.14	0.12	0.14	0.15	0.14

TABLE A2

Microprobe analyses of primary olivines in the serpentinized dunite of the Al-Wask ophiolite

Sample No.	W26										W54							
SiO_2	40.648	41.335	40.970	41.36	41.21	40.409	41.085	40.833	40.992	40.829	41.365	41.17	40.87	41.012	40.725	40.57	41.55	40.952
TiO_2	0.005	0.017	0	0.007	0.011	0.003	0	0.002	0.012	0	0.009	0	0.014	0.005	0	0	0.005	0.005
Al_2O_3	0.004	0	0	0.008	0	0.004	0.015	0	0.016	0.022	0.005	0.012	0.007	0.012	0	0	0.007	0.004
Cr_2O_3	0.007	0.012	0.007	0.013	0.013	0.028	0.003	0	0.028	0.013	0.01	0.1	0.038	0.016	0	0.015	0.01	0.016
FeO	8.41	8.042	7.092	7.846	8.157	7.616	8.232	8.292	8.392	8.247	8.198	8.167	8.117	8.289	8.162	8.157	8.206	8.261
MnO	0.156	0.12	0.108	0.104	0.153	0.125	0.115	0.132	0.139	0.14	0.12	0.109	0.117	0.134	0.138	0.127	0.153	0.134
MgO	50.626	50.181	51.424	49.211	50.291	50.866	50.046	50.26	50.61	50.09	49.974	49.796	49.921	50.137	49.881	50.216	49.511	50.227
CaO	0.024	0.037	0.023	0.024	0.036	0.031	0.044	0.037	0.008	0.028	0.029	0.029	0.038	0.033	0.028	0.042	0.026	0.029
NiO	0.465	0.472	0.458	0.426	0.431	0.449	0.461	0.515	0.505	0.471	0.417	0.39	0.5	0.491	0.426	0.415	0.436	0.45
Total	100.345	100.216	100.082	99.00	100.3	99.531	100.001	100.071	100.702	99.84	100.127	99.77	99.62	100.129	99.360	99.54	99.90	100.078
Si	0.989	1.004	0.993	1.014	1.001	0.988	1.001	0.996	0.993	0.997	1.005	1.004	1.000	0.999	0.999	0.994	1.012	0.998
Ti	0.000	0.000	0.000	0.000	0.000	0.000	0.000	0.000	0.000	0.000	0.000	0.000	0.000	0.000	0.000	0.000	0.000	0.000
Al	0.000	0.000	0.000	0.000	0.000	0.000	0.000	0.000	0.000	0.001	0.000	0.000	0.000	0.000	0.000	0.000	0.000	0.000
Cr	0.000	0.000	0.000	0.000	0.000	0.001	0.000	0.000	0.001	0.000	0.000	0.002	0.001	0.000	0.000	0.000	0.000	0.000
Fe(ii)	0.171	0.163	0.144	0.161	0.166	0.156	0.168	0.169	0.170	0.168	0.167	0.167	0.166	0.169	0.167	0.167	0.167	0.168
Mn	0.003	0.002	0.002	0.002	0.003	0.003	0.002	0.003	0.003	0.003	0.002	0.002	0.002	0.003	0.003	0.003	0.003	0.003
Mg	1.837	1.817	1.858	1.799	1.821	1.855	1.818	1.827	1.828	1.824	1.811	1.811	1.820	1.820	1.824	1.834	1.797	1.824
Ni	0.009	0.009	0.009	0.008	0.008	0.009	0.009	0.010	0.010	0.009	0.008	0.008	0.010	0.010	0.008	0.008	0.009	0.009
Ca	0.001	0.001	0.001	0.001	0.001	0.001	0.001	0.001	0.000	0.001	0.001	0.001	0.001	0.001	0.001	0.001	0.001	0.001
Endmembers																		
Fo	91.33	91.64	92.72	91.69	91.52	92.13	91.44	91.41	91.36	91.41	91.46	91.47	91.53	91.39	91.46	91.53	91.35	91.43
Fa	8.51	8.24	7.17	8.20	8.33	7.74	8.44	8.46	8.50	8.44	8.42	8.41	8.35	8.47	8.39	8.34	8.49	8.43
Tp	0.16	0.12	0.11	0.11	0.16	0.13	0.12	0.14	0.14	0.15	0.12	0.11	0.12	0.14	0.14	0.13	0.16	0.14

TABLE A3

Microprobe analyses of chromian spinels and their alteration products in the serpentinized harzburgite of the Al-Wask ophiolite

| Mineral | Chrome spinel | | | | | | | | | | | | | | | | |
Sample No.	W12									W57							
SiO_2	0.049	0.051	0.043	0.002	0.007	0.017	0.067	0.002	0.021	0.005	0.081	0.048	0.002	0.025	0.053	0.002	0.046
TiO_2	0.012	0.376	0.323	0.274	0.264	0.284	0.267	0.022	0.005	0.012	0.013	0.020	0.012	0.078	0.323	0.192	0.019
Al_2O_3	18.061	20.566	19.768	17.669	16.293	15.481	19.148	19.242	17.866	17.312	18.594	18.931	18.163	20.117	16.780	19.017	18.868
Cr_2O_3	51.331	44.331	45.643	45.987	45.865	48.064	46.579	49.927	50.535	51.428	49.641	50.234	50.682	51.178	46.393	48.369	49.328
FeO	20.561	21.289	19.692	21.563	24.285	23.279	20.541	20.111	21.066	20.901	20.276	20.944	18.630	17.366	23.975	19.817	21.268
MnO	0.235	0.472	0.870	0.770	0.841	0.835	0.425	0.194	0.188	0.152	0.197	0.258	0.157	0.161	0.986	0.313	0.211
MgO	9.514	11.501	12.337	12.423	10.825	10.994	12.312	10.157	10.021	10.188	10.597	9.271	11.047	10.553	11.169	11.505	10.157
NiO	0.063	0.150	0.077	0.050	0.092	0.067	0.118	0.049	0.093	0.099	0.027	0.050	0.036	0.032	0.077	0.099	0.049
Total	99.826	98.736	98.753	98.737	98.472	99.021	99.456	99.704	99.795	100.097	99.426	99.756	98.729	99.510	99.756	99.314	99.946
Ti	0.000	0.009	0.008	0.007	0.006	0.007	0.006	0.001	0.000	0.000	0.000	0.000	0.000	0.002	0.008	0.005	0.000
Al	0.683	0.765	0.734	0.660	0.620	0.588	0.708	0.721	0.673	0.652	0.699	0.715	0.685	0.751	0.629	0.709	0.707
Cr	1.302	1.106	1.136	1.153	1.171	1.225	1.156	1.255	1.278	1.298	1.251	1.272	1.283	1.283	1.167	1.209	1.239
$Fe3+$	0.014	0.111	0.115	0.174	0.196	0.173	0.123	0.022	0.049	0.050	0.050	0.012	0.031	-0.038	0.188	0.073	0.053
$Fe2+$	0.537	0.451	0.403	0.397	0.460	0.454	0.416	0.512	0.515	0.509	0.491	0.549	0.468	0.498	0.449	0.451	0.512
Mn	0.006	0.013	0.023	0.021	0.023	0.023	0.011	0.005	0.005	0.004	0.005	0.007	0.004	0.004	0.027	0.008	0.006
Ni	0.002	0.004	0.002	0.001	0.002	0.002	0.003	0.001	0.002	0.003	0.001	0.001	0.001	0.001	0.002	0.003	0.001
Mg	0.455	0.541	0.579	0.587	0.521	0.528	0.576	0.482	0.478	0.485	0.504	0.443	0.527	0.499	0.530	0.542	0.481
Cr#	0.66	0.59	0.61	0.64	0.65	0.68	0.62	0.64	0.65	0.67	0.64	0.64	0.65	0.63	0.65	0.63	0.64
Mg#	0.46	0.55	0.59	0.60	0.53	0.54	0.58	0.48	0.48	0.49	0.51	0.45	0.53	0.50	0.54	0.55	0.48
Fe^{3+}#	0.01	0.06	0.06	0.09	0.10	0.09	0.06	0.01	0.02	0.02	0.02	0.01	0.02	-0.02	0.09	0.04	0.03

TABLE A3
(continued)

| Mineral | Ferritchromite | | | | | | | Cr-magnetite | | | | |
Sample No.	W12				W57			W12			W57	
SiO$_2$	0.290	0.145	0.112	0.220	0.178	0.144	0.180	0.043	0.037	0.031	0.054	0.161
TiO$_2$	0.081	0.235	0.146	0.084	0.107	0.098	0.129	0.023	0.014	0.006	0.026	0.010
Al$_2$O$_3$	1.527	0.374	2.502	0.716	2.182	1.081	1.007	0.258	0.044	0.041	0.117	0.087
Cr$_2$O$_3$	36.066	24.635	40.205	32.807	38.735	36.826	31.730	5.656	6.344	3.003	4.419	2.211
FeO	55.077	69.248	49.770	59.461	50.034	51.862	61.114	84.894	86.451	90.493	86.484	89.464
MnO	1.288	1.721	1.353	1.608	1.463	1.464	1.488	0.443	0.241	0.217	0.423	0.186
MgO	2.528	0.674	3.117	1.357	3.201	3.800	1.388	2.456	0.842	0.904	1.973	1.211
NiO	0.118	0.128	0.253	0.167	0.246	0.264	0.104	0.392	0.661	0.899	0.528	0.571
Total	96.986	97.008	97.458	96.420	96.147	95.538	97.152	94.164	94.634	95.593	94.024	93.901
Ti	0.002	0.007	0.004	0.002	0.003	0.003	0.004	0.001	0.000	0.000	0.001	0.000
Al	0.066	0.016	0.107	0.032	0.095	0.047	0.044	0.011	0.002	0.002	0.005	0.004
Cr	1.051	0.725	1.156	0.972	1.130	1.079	0.930	0.167	0.190	0.089	0.132	0.066
Fe3+	0.878	1.245	0.728	0.992	0.770	0.868	1.018	1.820	1.808	1.909	1.862	1.929
Fe2+	0.820	0.911	0.786	0.871	0.774	0.739	0.877	0.838	0.925	0.916	0.861	0.908
Mn	0.040	0.054	0.042	0.051	0.046	0.046	0.047	0.014	0.008	0.007	0.013	0.006
Ni	0.004	0.004	0.007	0.005	0.007	0.008	0.003	0.012	0.020	0.027	0.016	0.017
Mg	0.139	0.037	0.169	0.076	0.176	0.210	0.077	0.137	0.047	0.050	0.111	0.068
Cr#	0.94	0.98	0.92	0.97	0.92	0.96	0.95	0.94	0.99	0.98	0.96	0.94
Mg#	0.14	0.04	0.18	0.08	0.19	0.22	0.08	0.14	0.05	0.05	0.11	0.07
Fe^{3+}#	0.44	0.63	0.37	0.50	0.39	0.44	0.51	0.91	0.90	0.95	0.93	0.96

TABLE A4

Microprobe analyses of chromian spinels and their alteration producrs in the serpentinized dunite of the Al-Wask ophiolite

Mineral	Chrome spinel												
Sample No.	W26							W54					
SiO$_2$	0.042	0.000	0.007	0.017	0.067	0.049	0.041	0.043	0.018	0.015	0.061	0.041	0.018
TiO$_2$	0.376	0.370	0.351	0.029	0.052	0.041	0.028	0.038	0.080	0.037	0.007	0.008	0.005
Al$_2$O$_3$	17.537	18.374	17.474	19.505	18.394	19.051	18.461	19.070	18.570	17.689	19.016	19.662	20.658
Cr$_2$O$_3$	48.552	48.056	48.664	52.088	51.957	51.539	52.315	51.050	50.307	51.853	51.040	50.090	50.024
FeO	20.641	20.127	20.003	17.350	21.623	21.392	21.907	20.655	24.402	23.896	18.121	19.605	18.540
MnO	1.033	0.919	1.014	0.150	0.340	0.402	0.370	0.350	0.488	0.406	0.215	0.235	0.186
MgO	11.090	11.014	11.315	10.230	7.171	7.255	7.037	8.142	6.278	6.038	11.269	9.858	9.925
NiO	0.097	0.024	0.037	0.063	0.020	0.045	0.003	0.000	0.009	0.019	0.061	0.078	0.072
Total	99.367	98.884	98.864	99.431	99.623	99.773	100.161	99.348	100.152	99.953	99.790	99.576	99.428
Ti	0.009	0.009	0.008	0.001	0.001	0.001	0.001	0.001	0.002	0.001	0.000	0.000	0.000
Al	0.659	0.691	0.659	0.733	0.708	0.730	0.707	0.728	0.714	0.686	0.708	0.739	0.774
Cr	1.224	1.213	1.230	1.313	1.341	1.324	1.345	1.308	1.298	1.348	1.275	1.262	1.257
Fe3+	0.099	0.078	0.094	-0.047	-0.052	-0.056	-0.054	-0.038	-0.017	-0.036	0.017	-0.001	-0.031
Fe2+	0.451	0.459	0.441	0.509	0.642	0.637	0.649	0.598	0.683	0.693	0.462	0.524	0.523
Mn	0.028	0.025	0.027	0.004	0.009	0.011	0.010	0.010	0.014	0.011	0.006	0.006	0.005
Ni	0.002	0.001	0.001	0.002	0.001	0.001	0.000	0.000	0.000	0.001	0.002	0.002	0.002
Mg	0.527	0.524	0.539	0.486	0.349	0.351	0.341	0.393	0.306	0.296	0.531	0.468	0.470
Cr#	0.65	0.64	0.65	0.64	0.65	0.64	0.66	0.64	0.65	0.66	0.64	0.63	0.62
Mg#	0.54	0.53	0.55	0.49	0.35	0.36	0.34	0.40	0.31	0.30	0.53	0.47	0.47
Fe^{3+}#	0.05	0.04	0.05	-0.02	-0.03	-0.03	-0.03	-0.02	-0.01	-0.02	0.01	0.00	-0.02

TABLE A4
(continued)

| Mineral Sample No. | Ferrichromite | | | | | | | | Cr-magnetite | | | | | | | |
	W26				W54				W26				W54			
SiO$_2$	0.215	0.153	0.245	0.246	0.189	0.143	0.142	0.209	0.078	0.104	0.110	0.043	0.037	0.041	0.054	0.061
TiO$_2$	0.126	0.040	0.163	0.128	0.058	0.011	0.083	0.084	0.005	0.023	0.025	0.021	0.008	0.020	0.015	0.007
Al$_2$O$_3$	2.139	7.681	4.035	2.388	1.427	2.413	1.838	1.948	0.058	0.037	0.096	0.243	0.014	0.041	0.041	0.051
Cr$_2$O$_3$	38.356	43.061	41.052	38.435	31.741	32.792	39.864	36.003	7.359	10.325	12.276	17.106	1.225	1.756	1.536	4.020
FeO	50.106	47.553	46.561	49.467	57.613	56.293	52.334	56.119	84.482	82.793	79.797	73.606	90.547	87.935	90.509	88.417
MnO	1.633	1.656	1.624	1.507	1.584	1.394	1.552	1.420	0.190	0.325	0.490	0.947	0.128	0.207	0.162	0.110
MgO	3.317	2.807	2.452	3.977	2.827	2.392	2.240	2.580	1.208	0.600	0.994	2.460	1.419	0.766	1.161	0.746
NiO	0.188	0.078	0.071	0.204	0.293	0.451	0.107	0.058	0.670	0.428	0.415	0.550	0.549	0.616	0.461	0.472
Total	96.080	103.027	96.203	96.352	95.732	95.889	98.159	98.420	94.050	94.634	94.202	94.975	93.928	91.382	93.939	93.884
Ti	0.003	0.001	0.005	0.004	0.002	0.000	0.002	0.002	0.000	0.001	0.001	0.001	0.000	0.001	0.000	0.000
Al	0.093	0.307	0.175	0.103	0.062	0.105	0.079	0.083	0.003	0.002	0.004	0.011	0.001	0.002	0.002	0.002
Cr	1.119	1.153	1.197	1.111	0.932	0.961	1.150	1.031	0.221	0.310	0.370	0.505	0.037	0.054	0.046	0.121
Fe3+	0.781	0.538	0.619	0.779	1.002	0.933	0.767	0.882	1.776	1.687	1.625	1.483	1.962	1.943	1.951	1.876
Fe2+	0.764	0.810	0.817	0.734	0.787	0.811	0.829	0.818	0.905	0.943	0.916	0.817	0.900	0.930	0.916	0.940
Mn	0.051	0.048	0.051	0.047	0.050	0.044	0.048	0.044	0.006	0.010	0.016	0.030	0.004	0.007	0.005	0.004
Ni	0.006	0.002	0.002	0.006	0.009	0.013	0.003	0.002	0.020	0.013	0.013	0.017	0.017	0.019	0.014	0.014
Mg	0.182	0.142	0.135	0.217	0.157	0.132	0.122	0.139	0.068	0.034	0.056	0.137	0.080	0.045	0.066	0.042
Cr#	0.92	0.79	0.87	0.92	0.94	0.90	0.94	0.93	0.99	0.99	0.99	0.98	0.98	0.97	0.96	0.98
Mg#	0.19	0.15	0.14	0.23	0.17	0.14	0.13	0.15	0.07	0.03	0.06	0.14	0.08	0.05	0.07	0.04
Fe^{3+}#	0.39	0.27	0.31	0.39	0.50	0.47	0.38	0.44	0.89	0.84	0.81	0.74	0.98	0.97	0.98	0.94

TABLE A5

Microprobe analyses of chromian spinels and their alteration products in the magnesite associated with the Al-Wask ophiolite

Mineral	Chrome spinel															
Sample No.	MW-5								MW-14							
SiO_2	0.014	0.000	0.013	0.121	0.014	0.008	0.023	0.000	0.021	0.001	0.000	0.033	0.011	0.041	0.036	0.025
TiO_2	0.097	0.313	0.025	0.028	0.019	0.082	0.088	0.116	0.000	0.008	0.000	0.023	0.006	0.011	0.036	0.062
Al_2O_3	17.449	16.512	18.565	14.437	17.699	17.244	12.642	17.063	16.473	16.363	15.607	13.205	16.729	13.811	17.407	12.836
Cr_2O_3	52.166	51.892	52.396	52.328	52.775	52.838	54.078	52.243	52.304	52.229	51.787	54.203	52.328	53.031	51.237	54.564
FeO	16.017	16.312	14.895	18.868	17.759	16.369	19.207	16.255	19.256	18.069	20.847	19.640	17.469	19.680	18.356	20.995
MnO	0.193	0.684	0.142	0.186	0.145	0.180	0.464	0.201	0.134	0.164	0.135	0.163	0.164	0.174	0.365	0.365
MgO	13.282	13.191	13.188	12.914	12.739	13.469	13.458	13.452	12.158	12.696	12.309	12.351	13.420	12.802	12.723	11.970
NiO	0.072	0.091	0.049	0.057	0.051	0.066	0.023	0.091	0.119	0.093	0.063	0.089	0.028	0.048	0.030	0.036
Total	99.290	98.995	99.274	98.939	101.200	100.257	99.983	99.420	100.465	99.621	100.748	99.706	100.155	99.597	100.195	100.853
Ti	0.002	0.007	0.001	0.001	0.000	0.002	0.002	0.003	0.000	0.000	0.000	0.001	0.000	0.000	0.001	0.001
Al	0.647	0.617	0.687	0.545	0.648	0.634	0.474	0.632	0.612	0.610	0.579	0.499	0.617	0.520	0.643	0.483
Cr	1.298	1.300	1.300	1.325	1.296	1.304	1.361	1.299	1.303	1.306	1.289	1.375	1.295	1.339	1.270	1.376
$Fe3+$	0.050	0.069	0.012	0.128	0.056	0.058	0.161	0.063	0.085	0.083	0.132	0.124	0.088	0.141	0.085	0.138
$Fe2+$	0.372	0.364	0.379	0.377	0.406	0.369	0.350	0.364	0.422	0.395	0.417	0.403	0.369	0.385	0.396	0.422
Mn	0.005	0.018	0.004	0.005	0.004	0.005	0.013	0.005	0.004	0.004	0.004	0.004	0.004	0.005	0.010	0.010
Ni	0.002	0.002	0.001	0.001	0.001	0.002	0.001	0.002	0.003	0.002	0.002	0.002	0.001	0.001	0.001	0.001
Mg	0.623	0.623	0.617	0.617	0.590	0.627	0.639	0.631	0.571	0.599	0.578	0.591	0.626	0.609	0.595	0.569
$Cr\#$	0.67	0.68	0.65	0.71	0.67	0.67	0.74	0.67	0.68	0.68	0.69	0.73	0.68	0.72	0.66	0.74
$Mg\#$	0.63	0.63	0.62	0.62	0.59	0.63	0.65	0.63	0.57	0.60	0.58	0.59	0.63	0.61	0.60	0.57
$Fe^{3+}\#$	0.02	0.03	0.01	0.06	0.03	0.03	0.08	0.03	0.04	0.04	0.07	0.06	0.04	0.07	0.04	0.07

Table A5
(continued)

Mineral	Ferrichromite						Cr-magnetite			
Sample No.	MW-5				MW-14		Mw-5		MW-14	
SiO$_2$	0.147	0.205	0.183	0.161	0.142	0.201	0.088	0.104	0.074	0.076
TiO$_2$	0.257	0.133	0.160	0.140	0.403	0.601	0.009	0.000	0.016	0.009
Al$_2$O$_3$	1.516	1.403	1.579	0.720	4.208	2.791	0.078	0.026	0.055	0.042
Cr$_2$O$_3$	45.496	46.689	43.800	42.314	48.133	51.513	2.496	4.302	5.298	6.508
FeO	39.480	41.964	40.289	46.425	38.749	36.585	88.573	86.715	87.231	85.833
MnO	1.073	0.889	1.151	1.178	0.994	0.627	0.276	0.298	0.172	0.193
MgO	7.105	4.678	4.471	4.855	4.024	5.266	1.002	0.893	0.863	0.852
NiO	0.237	0.245	0.212	0.108	0.084	0.065	0.455	1.141	0.485	0.528
Total	95.313	96.206	91.844	95.902	96.737	97.649	92.977	93.479	94.195	94.041
Ti	0.007	0.004	0.005	0.004	0.011	0.016	0.000	0.000	0.000	0.000
Al	0.065	0.061	0.071	0.031	0.180	0.118	0.004	0.001	0.002	0.002
Cr	1.305	1.356	1.330	1.231	1.382	1.463	0.076	0.130	0.159	0.196
Fe3+	0.616	0.576	0.589	0.730	0.416	0.386	1.920	1.869	1.838	1.802
Fe2+	0.583	0.713	0.705	0.698	0.760	0.713	0.920	0.904	0.931	0.930
Mn	0.033	0.028	0.037	0.037	0.031	0.019	0.009	0.010	0.006	0.006
Ni	0.007	0.007	0.007	0.003	0.002	0.002	0.014	0.035	0.015	0.016
Mg	0.384	0.256	0.256	0.266	0.218	0.282	0.057	0.051	0.049	0.048
Cr#	0.95	0.96	0.95	0.98	0.88	0.93	0.96	0.99	0.98	0.99
Mg#	0.40	0.26	0.27	0.28	0.22	0.28	0.06	0.05	0.05	0.05
Fe^{3+}#	0.31	0.29	0.30	0.37	0.21	0.20	0.96	0.93	0.92	0.90

TABLE A6

Microprobe analyses of serpentine minerals of the serpentinized harzbergite and dunite of the Al-Wask ophiolite

Rock type	Serpentinized harzburgite																		
Sample No.	W12									W57									
Spot No.	#1	#2	#3	#4	#5	#6	#7	#8	#9	#1	#2	#3	#4	#5	#6	#7	#8	#9	#10
SiO_2	43.898	44.209	43.677	44.156	43.251	44.064	44.113	43.862	44.561	44.159	44.376	44.290	44.583	43.906	43.786	43.756	44.555	44.501	43.575
TiO_2	0.004	0.007	0.023	0.024	0.025	0.018	0.007	0.007	0.005	0.009	0.004	0.014	0.000	0.005	0.018	0.019	0.013	0.005	0.015
Al_2O_3	0.015	0.467	0.130	0.475	0.212	0.537	0.185	0.300	0.275	0.322	0.054	0.555	0.342	0.015	0.387	0.243	0.071	0.198	0.323
Cr_2O_3	0.207	0.017	0.090	0.009	0.007	0.015	0.155	0.004	0.019	0.019	0.018	0.013	0.005	0.020	0.171	0.031	0.049	0.012	0.067
FeO	1.942	1.898	1.833	1.756	1.956	1.753	1.951	1.893	1.715	1.836	1.842	1.629	1.958	1.822	1.902	1.749	3.058	1.710	3.258
MnO	0.003	0.000	0.000	0.000	0.000	0.005	0.003	0.006	0.000	0.005	0.000	0.004	0.003	0.002	0.000	0.001	0.097	0.000	0.029
MgO	40.931	39.896	40.997	39.581	40.771	39.560	40.619	39.758	40.681	39.707	40.847	39.726	40.147	41.101	40.415	40.564	38.200	40.765	38.600
CaO	0.047	0.014	0.036	0.035	0.032	0.027	0.036	0.023	0.010	0.006	0.018	0.020	0.032	0.043	0.029	0.030	0.040	0.014	0.073
Total	87.047	86.508	86.787	86.037	86.254	85.980	87.070	85.854	87.266	86.063	87.158	86.250	87.070	86.913	86.707	86.393	86.082	87.204	85.941
Structural Formulae																			
Si	2.041	2.058	2.034	2.065	2.027	2.062	2.048	2.059	2.056	2.066	2.053	2.064	2.063	2.040	2.041	2.043	2.095	2.055	2.059
Al	0.001	0.026	0.007	0.026	0.012	0.030	0.010	0.017	0.015	0.018	0.003	0.030	0.019	0.001	0.021	0.013	0.004	0.011	0.018
Ti	0.000	0.000	0.001	0.001	0.001	0.001	0.000	0.000	0.000	0.000	0.000	0.000	0.000	0.000	0.001	0.001	0.000	0.000	0.001
Fe(ii)	0.076	0.074	0.071	0.069	0.077	0.069	0.076	0.074	0.066	0.072	0.071	0.063	0.076	0.071	0.074	0.068	0.120	0.066	0.129
Mn	0.000	0.000	0.000	0.000	0.000	0.000	0.000	0.000	0.000	0.000	0.000	0.000	0.000	0.000	0.000	0.000	0.004	0.000	0.001
Mg	2.838	2.769	2.846	2.759	2.849	2.760	2.811	2.782	2.798	2.769	2.817	2.760	2.769	2.846	2.809	2.823	2.678	2.807	2.720
Ca	0.002	0.001	0.002	0.002	0.002	0.001	0.002	0.001	0.000	0.000	0.001	0.001	0.002	0.002	0.001	0.002	0.002	0.001	0.004

TABLE A6
(continued)

Rock type	Serpentinized dunite																
Sample No.	W26									W54							
Spot No.	#1	#2	#3	#4	#5	#6	#7	#8	#9	#1	#2	#2	#4	#5	#6	#7	#8
SiO₂	44.013	43.654	44.191	43.514	43.087	43.392	43.718	43.392	43.383	43.879	43.476	44.234	43.733	44.483	44.036	43.788	43.794
TiO₂	0.011	0.032	0.021	0.023	0.009	0.019	0.029	0.021	0.018	0.024	0.027	0.013	0.022	0.009	0.016	0.015	0.012
Al₂O₃	0.255	0.131	0.306	0.230	0.315	0.282	0.341	0.352	0.394	0.213	0.231	0.408	0.323	0.486	0.094	0.397	0.357
Cr₂O₃	0.104	0.071	0.038	0.050	0.104	0.059	0.031	0.061	0.023	0.112	0.050	0.086	0.033	0.103	0.040	0.130	0.039
FeO	2.957	2.992	3.049	3.347	3.130	2.199	3.077	4.993	3.413	3.410	2.583	4.658	3.317	1.947	3.756	1.903	2.920
MnO	0.017	0.045	0.040	0.017	0.040	0.002	0.055	0.049	0.033	0.000	0.000	0.036	0.050	0.003	0.017	0.007	0.008
MgO	38.693	38.694	38.726	38.648	38.771	39.545	38.311	37.922	39.324	38.751	39.497	38.183	38.420	39.747	38.712	39.643	38.506
CaO	0.032	0.087	0.028	0.076	0.078	0.074	0.061	0.068	0.053	0.064	0.106	0.025	0.025	0.014	0.100	0.024	0.044
Total	86.083	85.707	86.398	85.905	85.533	85.571	85.623	86.858	86.641	86.452	85.969	87.642	85.925	86.792	86.771	85.906	85.680
Structural Formulae																	
Si	2.072	2.066	2.072	2.058	2.048	2.050	2.069	2.049	2.037	2.063	2.049	2.063	2.066	2.066	2.066	2.057	2.069
Al	0.014	0.007	0.017	0.013	0.018	0.016	0.019	0.020	0.022	0.012	0.013	0.022	0.018	0.027	0.005	0.022	0.020
Ti	0.000	0.001	0.001	0.001	0.000	0.001	0.001	0.001	0.001	0.001	0.001	0.000	0.001	0.000	0.001	0.001	0.000
Fe(ii)	0.116	0.118	0.120	0.132	0.124	0.087	0.122	0.197	0.134	0.134	0.102	0.182	0.131	0.076	0.147	0.075	0.115
Mn	0.001	0.002	0.002	0.001	0.002	0.000	0.002	0.002	0.001	0.000	0.000	0.001	0.002	0.000	0.001	0.000	0.000
Mg	2.715	2.730	2.707	2.725	2.747	2.785	2.704	2.669	2.753	2.717	2.775	2.655	2.706	2.752	2.707	2.776	2.713
Ca	0.002	0.004	0.001	0.004	0.004	0.004	0.003	0.003	0.003	0.003	0.005	0.001	0.001	0.001	0.005	0.001	0.002

TABLE A7

Microprobe analyses of amphiboles of the serpentinized harzburgite and dunite of the Al-Wask ophiolite

Rock type	Serpentinized harzburgite																			
	harzburgite	W12				W57				W26							W54			
Sample No.																				
SiO_2	56.441	56.344	54.295	55.703	56.372	54.506	55.182	56.447	55.414	56.209	56.591	56.282	56.347	55.373	55.619	55.378	55.689	55.602	56.355	55.841
TiO_2	0.027	0.028	0.062	0.018	0.035	0.112	0.042	0.030	0.025	0.052	0.030	0.032	0.017	0.026	0.030	0.063	0.034	0.039	0.032	0.045
Al_2O_3	0.951	1.053	1.221	0.912	1.013	2.340	1.478	1.053	0.922	1.584	0.799	1.000	0.920	1.007	1.101	1.639	1.450	1.144	1.124	0.943
Cr_2O_3	0.106	0.139	0.245	0.137	0.100	0.307	0.207	0.127	0.086	0.110	0.111	0.146	0.159	0.053	0.101	0.125	0.080	0.147	0.157	0.109
FeO	2.929	2.430	3.654	3.045	2.629	3.458	3.374	2.984	3.413	2.973	2.543	3.163	2.600	3.382	3.237	3.581	3.259	3.422	2.267	3.253
MnO	0.062	0.057	0.112	0.070	0.061	0.104	0.102	0.039	0.072	0.105	0.050	0.065	0.069	0.070	0.049	0.146	0.051	0.069	0.063	0.058
MgO	23.334	23.115	22.059	23.267	23.203	22.528	22.503	23.532	23.450	23.275	23.412	22.895	23.606	23.336	23.008	22.727	23.462	22.949	23.207	23.518
CaO	12.432	12.288	11.818	12.521	12.753	11.466	12.067	12.644	11.561	11.902	12.238	12.456	12.469	11.528	11.907	11.719	11.897	12.127	12.740	11.955
Na_2O	0.336	0.396	0.612	0.400	0.371	0.786	0.638	0.331	0.397	0.373	0.408	0.441	0.343	0.563	0.505	0.421	0.633	0.545	0.424	0.425
K_2O	0.002	0.008	0.042	0.001	0.002	0.050	0.029	0.005	0.001	0.016	0.003	0.008	0.004	0.004	0.011	0.024	0.007	0.012	0.003	0.004
Total	96.575	96.240	94.120	95.693	96.633	95.656	95.622	97.054	95.343	96.599	96.228	96.489	96.441	95.343	95.569	95.824	96.562	96.056	96.509	96.151
Structural formulae																				
Si	7.779	7.813	7.710	7.738	7.779	7.608	7.705	7.743	7.740	7.738	7.821	7.775	7.773	7.736	7.753	7.702	7.690	7.725	7.785	7.739
Al iv	0.154	0.172	0.204	0.149	0.165	0.385	0.243	0.170	0.152	0.257	0.130	0.163	0.150	0.166	0.181	0.269	0.236	0.187	0.183	0.154
Al vi	0.000	0.000	0.000	0.000	0.000	0.000	0.000	0.000	0.000	0.000	0.000	0.000	0.000	0.000	0.000	0.000	0.000	0.000	0.000	0.000
Ti	0.003	0.003	0.007	0.002	0.004	0.012	0.004	0.003	0.003	0.005	0.003	0.003	0.002	0.003	0.003	0.007	0.004	0.004	0.003	0.005
Cr	0.012	0.015	0.028	0.015	0.011	0.034	0.023	0.014	0.010	0.012	0.012	0.016	0.017	0.006	0.011	0.014	0.009	0.016	0.017	0.012
Fe^{3+}	0.338	0.282	0.434	0.354	0.303	0.404	0.394	0.342	0.399	0.342	0.294	0.365	0.300	0.395	0.377	0.417	0.376	0.398	0.262	0.377
Mn	0.007	0.007	0.014	0.008	0.007	0.012	0.012	0.005	0.009	0.012	0.006	0.008	0.008	0.008	0.006	0.017	0.006	0.008	0.007	0.007
Mg	4.794	4.778	4.670	4.818	4.773	4.688	4.684	4.812	4.883	4.777	4.824	4.715	4.854	4.861	4.781	4.712	4.830	4.753	4.780	4.859
Ca	1.836	1.826	1.798	1.863	1.886	1.715	1.805	1.858	1.730	1.756	1.812	1.844	1.843	1.726	1.778	1.746	1.760	1.805	1.886	1.775
Na	0.090	0.107	0.168	0.108	0.099	0.213	0.173	0.088	0.108	0.099	0.109	0.118	0.092	0.152	0.136	0.114	0.169	0.147	0.113	0.114
K	0.000	0.001	0.008	0.000	0.000	0.009	0.005	0.001	0.000	0.003	0.000	0.001	0.001	0.001	0.002	0.004	0.001	0.002	0.001	0.001
Amphibole names	tremolite	tremolite				tremolite				tremolite							tremolite			

TABLE A8

Microprobe analyses of chlorites of the serpentinized harzburgite and dunite of the Al-Wask ophiolite

Green chlorite — Serpentinized harzburgite

	W57								W12										
Mineral																			
SiO₂	26.404	25.147	28.851	25.914	27.392	28.104	26.082	30.888	29.561	27.953	25.867	29.286	30.454	25.786	29.060	25.200	30.282	28.577	
TiO₂	0.037	0.021	0.025	0.037	0.006	0.036	0.053	0.030	0.312	0.012	0.010	0.252	0.360	0.034	0.037	0.052	0.075	0.028	0.053
Al₂O₃	21.612	20.824	19.714	20.900	21.350	20.255	20.393	13.723	17.388	21.056	20.774	17.109	17.756	20.924	17.329	20.746	17.130	18.452	20.712
Cr₂O₃	1.006	0.956	1.673	0.789	1.490	1.528	0.987	1.011	1.241	1.278	1.102	1.208	1.607	0.987	1.231	0.889	1.446	1.325	1.012
FeOT	22.877	29.615	14.315	27.346	12.260	14.541	27.337	8.790	19.143	13.451	26.545	14.651	18.619	26.607	19.575	27.892	17.754	17.270	30.249
MnO	0.128	0.104	0.050	0.076	0.079	0.047	0.099	0.007	0.012	0.080	0.061	0.012	0.008	0.092	0.009	0.107	0.010	0.053	0.140
MgO	15.319	12.185	21.033	12.988	23.461	21.826	12.348	31.164	18.314	22.493	13.473	21.160	18.369	12.999	19.404	12.937	20.142	19.748	12.593
CaO	0.018	0.013	0.014	0.032	0.022	0.028	0.000	0.353	0.013	0.097	0.046	0.075	0.016	0.331	0.013	0.338	0.190	0.050	0.351
Na₂O	0.038	0.006	0.006	0.021	0.005	0.013	0.020	0.043	0.009	0.016	0.021	0.016	0.009	0.050	0.018	0.059	0.035	0.013	0.052
K₂O	0.017	0.005	0.034	0.009	0.010	0.020	0.012	0.042	0.011	0.044	0.008	0.018	0.044	0.050	0.027	0.056	0.078	0.032	0.054
NiO		0.018	0.100	0.009	0.014	0.021	0.016	0.092	0.003	0.121	0.117	0.121	0.013	0.094	0.017	0.080	0.014	0.017	0.023
Total	87.456	88.895	85.814	88.120	86.090	86.417	87.347	86.141	86.006	86.599	88.025	83.907	87.255	87.954	86.718	88.355	87.154	85.566	65.239
Structural Formulae																			
Si	5.476	5.355	5.815	5.474	5.479	5.652	5.556	6.056	6.081	5.581	5.459	6.054	6.134	5.451	5.975	5.361	6.113	5.880	5.181
Al iv	2.524	2.645	2.185	2.526	2.521	2.348	2.444	1.944	1.919	2.419	2.541	1.946	1.866	2.549	2.025	2.639	1.887	2.120	2.819
Al vi	2.782	2.588	2.527	2.694	2.525	2.472	2.699	1.254	2.327	2.553	2.641	2.248	2.387	2.682	2.192	2.571	2.214	2.377	2.381
Ti	0.006	0.003	0.004	0.006	0.001	0.005	0.008	0.004	0.048	0.002	0.002	0.039	0.054	0.005	0.006	0.008	0.011	0.004	0.009
Cr	0.165	0.161	0.267	0.132	0.236	0.243	0.166	0.157	0.202	0.202	0.184	0.197	0.256	0.165	0.200	0.150	0.231	0.215	0.170
Fe³⁺	0.231	0.059	0.337	0.167	0.132	0.205	0.237	0.000	0.391	0.180	0.154	0.318	0.488	0.156	0.205	0.037	0.310	0.262	0.000
Fe²⁺	3.736	5.215	2.075	4.664	1.919	2.240	4.633	1.663	2.902	2.066	4.531	2.215	2.648	4.548	3.161	4.926	2.687	2.710	5.480
Mn	0.022	0.019	0.008	0.014	0.013	0.008	0.018	0.001	0.002	0.013	0.011	0.002	0.001	0.016	0.001	0.019	0.002	0.009	0.025
Mg	4.736	3.868	6.319	4.090	6.995	6.543	3.921	9.108	5.616	6.694	4.238	6.521	5.515	4.096	5.948	4.103	6.061	6.057	3.979
Ni	0.000	0.003	0.016	0.002	0.002	0.003	0.003	0.014	0.000	0.019	0.020	0.020	0.002	0.016	0.003	0.014	0.002	0.003	0.004
Ca	0.004	0.003	0.003	0.007	0.005	0.006	0.000	0.074	0.003	0.021	0.010	0.017	0.004	0.075	0.003	0.077	0.041	0.011	0.080
Na	0.031	0.005	0.005	0.017	0.004	0.010	0.017	0.033	0.007	0.012	0.017	0.013	0.007	0.041	0.014	0.048	0.027	0.010	0.043
K	0.009	0.003	0.017	0.005	0.005	0.010	0.006	0.021	0.006	0.022	0.004	0.009	0.023	0.027	0.014	0.030	0.040	0.017	0.029
Variety	ripido-lite	ripido-lite	pycno-chlorite	ripido-lite	ripido-lite	pycno-chlorite	ripido-lite	clino-chlore	pycno-chlorite	ripido-lite	ripido-lite	pycno-chlorite	pycno-chlorite	ripido-lite	pycno-chlorite	ripido-lite	pycno-chlorite	pycno-chlorite	ripid-olite
T °C	264	341	268	325	301	286	317	236	247	292	326	243	240	327	258	338	241	266	360

TABLE A8
(continued)

Green Chlorite

Serpentinized dunite

Mineral				W26								W54				
Sample No.																
SiO₂	29.739	27.569	30.199	25.750	30.359	25.806	29.715	30.160	27.526	27.343	29.667	27.403	30.095	27.465	30.409	28.169	30.492
TiO₂	0.247	0.022	0.395	0.134	0.382	0.020	0.316	0.182	0.018	0.030	0.415	0.015	0.292	0.029	0.189	0.031	0.046
Al₂O₃	17.241	20.611	17.948	21.179	16.746	21.037	14.991	14.207	20.718	21.219	14.690	20.415	13.781	20.443	14.320	18.025	14.391
Cr₂O₃	0.965	1.085	1.160	1.208	1.082	0.697	0.864	1.002	1.318	1.391	0.749	1.291	0.897	1.767	1.210	0.889	1.012
FeOT	19.528	12.979	20.033	24.866	19.394	22.991	9.251	9.560	12.801	13.783	7.875	12.957	9.520	12.517	8.956	13.601	8.622
MnO	0.017	0.112	0.016	0.078	0.017	0.123	0.008	0.011	0.088	0.077	0.009	0.102	0.008	0.119	0.006	0.053	0.007
MgO	18.733	22.711	18.014	14.792	18.569	16.196	30.584	31.239	22.753	21.638	30.571	22.829	30.911	23.247	31.064	25.379	31.105
CaO	0.017	0.203	0.020	0.005	0.012	0.003	0.294	0.350	0.015	0.019	0.244	0.014	0.200	0.028	0.308	0.020	0.347
Na₂O	0.006	0.031	0.007	0.018	0.009	0.019	0.040	0.041	0.011	0.020	0.026	0.006	0.055	0.016	0.054	0.023	0.041
K₂O	0.012	0.035	0.078	0.009	0.010	0.003	0.077	0.041	0.016	0.030	0.034	0.026	0.128	0.020	0.058	0.027	0.187
NiO	0.120	0.020	0.011	0.008	0.101	0.054	0.132	0.114	0.030	0.089	0.111	0.009	0.094	0.015	0.122	0.114	0.114
Total	86.626	85.379	87.881	88.046	86.681	86.949	86.273	86.906	85.294	85.638	84.391	85.067	85.981	85.667	86.697	86.331	86.365
Structural Formulae																	
Si	6.091	5.578	6.087	5.386	6.194	5.415	5.831	5.879	5.566	5.532	5.918	5.568	5.928	5.538	5.933	5.664	5.955
Al iv	1.909	2.422	1.913	2.614	1.806	2.585	2.169	2.121	2.434	2.468	2.082	2.432	2.072	2.462	2.067	2.336	2.045
Al vi	2.279	2.508	2.385	2.621	2.252	2.628	1.333	1.181	2.520	2.611	1.396	2.470	1.164	2.410	1.257	1.953	1.302
Ti	0.038	0.003	0.060	0.021	0.059	0.003	0.047	0.027	0.003	0.005	0.062	0.002	0.043	0.004	0.028	0.005	0.007
Cr	0.156	0.174	0.185	0.200	0.175	0.116	0.134	0.154	0.211	0.222	0.118	0.207	0.140	0.282	0.187	0.141	0.156
Fe³⁺	0.334	0.138	0.424	0.133	0.411	0.087	0.000	0.000	0.164	0.200	0.000	0.134	0.000	0.127	0.000	0.000	0.000
Fe²⁺	3.011	2.058	2.954	4.217	2.899	3.948	1.778	1.865	2.001	2.132	1.501	2.067	1.863	1.984	1.704	2.389	1.662
Mn	0.003	0.019	0.003	0.014	0.003	0.022	0.001	0.002	0.015	0.013	0.002	0.017	0.001	0.020	0.001	0.009	0.001
Mg	5.719	6.850	5.413	4.612	5.648	5.066	8.946	9.077	6.859	6.525	9.091	6.915	9.076	6.988	9.035	7.607	9.056
Ni	0.020	0.003	0.002	0.001	0.017	0.009	0.021	0.018	0.005	0.014	0.018	0.001	0.015	0.002	0.019	0.018	0.018
Ca	0.004	0.044	0.004	0.001	0.003	0.001	0.062	0.073	0.003	0.004	0.052	0.003	0.042	0.006	0.064	0.004	0.073
Na	0.005	0.025	0.006	0.015	0.007	0.015	0.030	0.031	0.009	0.015	0.020	0.005	0.042	0.013	0.041	0.018	0.031
K	0.006	0.018	0.040	0.005	0.005	0.002	0.039	0.020	0.008	0.015	0.017	0.013	0.064	0.010	0.029	0.014	0.093
Variety	pycno-chlorite	ripido-lite	pycno-chlorite	ripido-lite	pycno-chlorite	ripido-lite	clino-chlore	clino-chlore	ripido-lite	ripido-lite	clino-chlore	ripido-lite	clino-chlore	ripid-olite	clino-chlore	pycno-chlorite	clino-chlore
T °C	318	246	292	247	331	235	324	293	260	255	298	249	293	250	295	249	283

TABLE A8
(continued)

	Kämmererite											
Rock type	Serpentinized harzburgite											
Sample No.				W12						W57		
SiO₂	27.292	27.260	27.267	27.176	27.144	27.227	27.998	27.374	28.171	27.608	26.871	26.851
TiO₂	0.007	0.042	0.031	0.034	0.036	0.016	0.000	0.007	0.000	0.046	0.017	0.041
Al₂O₃	20.475	20.334	20.328	20.360	20.140	20.382	19.558	19.724	19.454	19.880	20.054	20.474
Cr₂O₃	3.066	3.592	3.277	3.401	2.803	2.890	2.912	3.631	2.482	3.133	3.665	3.425
FeOT	12.898	12.640	12.392	12.511	12.415	12.313	12.234	12.280	12.222	11.886	12.666	12.486
MnO	0.083	0.072	0.093	0.091	0.101	0.083	0.085	0.081	0.089	0.096	0.072	0.083
MgO	22.546	22.668	22.458	22.439	22.544	22.447	23.906	23.287	23.774	23.418	22.698	22.647
CaO	0.037	0.019	0.015	0.081	0.020	0.016	0.005	0.002	0.007	0.017	0.024	0.020
Na₂O	0.021	0.010	0.004	0.040	0.000	0.008	0.015	0.020	0.018	0.017	0.011	0.011
K₂O	0.034	0.020	0.015	0.071	0.041	0.020	0.011	0.228	0.012	0.026	0.009	0.009
NiO	0.021	0.026	0.025	0.018	0.019	0.022	0.011	0.014	0.008	0.018	0.021	0.014
Total	86.479	86.681	85.905	86.221	85.262	85.424	86.735	86.648	86.238	86.145	86.108	86.062
Structural Formulae												
Si	5.480	5.462	5.497	5.470	5.513	5.511	5.585	5.491	5.640	5.538	5.434	5.419
Al iv	2.520	2.538	2.503	2.530	2.487	2.489	2.415	2.509	2.360	2.462	2.566	2.581
Al vi	2.342	2.280	2.345	2.317	2.350	2.391	2.196	2.168	2.244	2.253	2.225	2.303
Ti	0.001	0.006	0.005	0.005	0.005	0.002	0.000	0.001	0.000	0.007	0.003	0.006
Cr	0.487	0.569	0.522	0.541	0.450	0.462	0.459	0.576	0.393	0.497	0.586	0.547
Fe3+	0.165	0.176	0.205	0.173	0.175	0.201	0.130	0.103	0.150	0.162	0.136	0.153
Fe2+	2.001	1.942	1.884	1.933	1.934	1.883	1.911	1.957	1.897	1.832	2.006	1.954
Mn	0.014	0.012	0.016	0.015	0.017	0.014	0.014	0.014	0.015	0.016	0.012	0.014
Mg	6.748	6.771	6.749	6.732	6.825	6.772	7.109	6.963	7.095	7.003	6.842	6.813
Ni	0.003	0.004	0.004	0.003	0.003	0.004	0.002	0.002	0.001	0.003	0.003	0.002
Ca	0.008	0.004	0.003	0.017	0.004	0.003	0.001	0.001	0.002	0.004	0.005	0.004
Na	0.016	0.008	0.003	0.031	0.000	0.006	0.012	0.016	0.014	0.013	0.008	0.008
K	0.017	0.010	0.008	0.036	0.021	0.010	0.006	0.116	0.006	0.013	0.005	0.005
Variety	ripidolite	ripidolite	ripidolite	ripidolite	ripidolite	ripidolite	ripidolite	ripidolite	pycnochlorite	ripidolite	ripidolite	ripidolite
T °C	246	302	304	300	303	298	298	290	300	284	294	307

REFERENCES

Abd El-Naby, H. H., and Frisch, W., 2002, Origin of the Wadi Haimur-Abu Swayel gneiss belt, south Eastern Desert, Egypt: Petrological and geochronological constraints: Precambrian Research, v. 113, n. 3–4, p. 307–322, https://doi.org/10.1016/S0301-9268(01)00214-5

Abdelsalam, M. G., and Stern, R. J., 1996, Sutures and shear zones in the Arabian–Nubian Shield: Journal of African Earth Sciences, v. 23, n. 3, p. 289–310, https://doi.org/10.1016/S0899-5362(97)00003-1

Abdelsalam, M. G., Abdeen, M. M., Dowaidar, H. M., Stern, R. J., and Abdelghaffar, A. A., 2003, Structural evolution of the Neoproterozoic Western Allaqi-Heiani suture, southeastern Egypt: Precambrian Research, v. 124, n. 1, p. 87–104, https://doi.org/10.1016/S0301-9268(03)00080-9

Agar, R. A., 1987, The Najd fault system revisited; a two-way strike-slip orogen in the Saudi Arabian Shield: Journal of Structural Geology, v. 9, n. 1, p. 41–48, https://doi.org/10.1016/0191-8141(87)90042-3

Ahmed, A. H., and Habtoor, A., 2015, Heterogeneously depleted Precambrian lithosphere deduced from mantle peridotites and associated chromitite deposits of Al'Ays ophiolite, Northwestern Arabian Shield, Saudi Arabia: Ore Geology Reviews, v. 67, p. 279–296, https://doi.org/10.1016/j.oregeorev.2014.12.018

Ahmed, A. H., and Surour, A. A., 2016, Fluid-related modifications of Cr-spinel and olivine from ophiolitic peridotites by contact metamorphism of granitic intrusions in the Ablah area, Saudi Arabia: Journal of Asian Earth Sciences, v. 122, p. 58–79, https://doi.org/10.1016/j.jseaes.2016.03.010

Ahmed, A. H., Harbi, H. M., and Habtoor, A. M., 2012, Compositional variations and tectonic settings of podiform chromitites and associated ultramafic rocks of the Neoproterozoic ophiolite at Wadi Al Hwanet, northwestern Saudi Arabia: Journal of Asian Earth Sciences, v. 56, p. 118–134, https://doi.org/10.1016/j.jseaes.2012.05.002

Ahmed, Z., and Hariri, M.M., 2008, Neoproterozoic ophiolites as developed in Saudi Arabia and their oceanic and pericontinental domains: Arabian Journal for Science and Engineering, v. 33, n. 1C, p. 17–54.

Ali, K. A., Azer, M. K., Gahlan, H. A., Wilde, S. A., Samuel, M. D., and Stern, R. J., 2010, Age constraints on the formation and emplacement of Neoproterozoic ophiolites along the Allaqi Suture, south Eastern Desert, Egypt: Gondwana Research, v. 18, n. 4, p. 583–595, https://doi.org/10.1016/j.gr.2010.03.002

Al-Shanti, A. M., and Gass, I. G., 1983, The upper Proterozoic ophiolite mélange zones of the easternmost Arabian shield: Journal of the Geological Society, London, v. 140, n. 6, p. 867–876, https://doi.org/10.1144/gsjgs.140.6.0867

Al-Shanti, M.M.S., ms, 1982, Geology and mineralization of the Ash Shizm-Jabal Ess area: Jeddah, Saudi Arabia, King Abdulaziz University, Ph. D. thesis, p. 291.

Arai, S., 1992, Chemistry of chromian spinel in volcanic rocks as a potential guide to magma chemistry: Mineralogical Magazine, v. 56, n. 383, p. 173–184, https://doi.org/10.1180/minmag.1992.056.383.04

—— 1994, Characterization of spinel peridotites by olivine-spinel compositional relationships: Review and interpretations: Chemical Geology, v. 113, n. 3–4, p. 191–204, https://doi.org/10.1016/0009-2541(94)90066-3

Azer, M. K., 2014, Petrological studies of Neoproterozoic serpentinized ultramafics of the Nubian Shield: Spinel compositions as evidence of the tectonic evolution of the Egyptian ophiolites: Acta Geologica Polonica, v. 64, n. 1, p. 113–127, https://doi.org/10.2478/agp-2014-0006

Azer, M. K., and El-Gharbawy, R. I., 2011, The Neoproterozoic layered mafic-ultramafic intrusion of Gabal Imleih, south Sinai, Egypt: Implication of post-collisional magmatism in the north Arabian-Nubian Shield: Journal of African Earth Sciences, v. 60, n. 4, p. 253–272, https://doi.org/10.1016/j.jafrearsci.2011.03.010

Azer, M. K., and Khalil, A. E. S., 2005, Petrological and mineralogical studies of Pan-African serpentinites at Bir Al-Edeid area, Central Eastern Desert, Egypt: Journal of African Earth Sciences, v. 43, p. 525–536, https://doi.org/10.1016/j.jafrearsci.2005.09.008

Azer, M. K., and Stern, R. J., 2007, Neoproterozoic (835–720 Ma) serpentinites in the Eastern Desert, Egypt: Fragments of fore-arc mantle: The Journal of Geology, v. 115, n. 4, p. 457–472, https://doi.org/10.1086/518052

Azer, M. K., Samuel, M. D., Ali, K. A., Gahlan, H. A., Stern, R. J., Ren, M., and Moussa, H. E., 2013, Neoproterozoic ophiolitic peridotites along the Allaqi-Heiani Suture, South Eastern Desert, Egypt: Mineralogy and Petrology, 107, p. 829–848, https://doi.org/10.1007/s00710-012-0204-z

Azer, M. K., Obeid, M. A., and Gahlan, H. A., 2016, Late Neoproterozoic layered mafic intrusion of arc-affinity in the Arabian-Nubian Shield: A case study from the Shahira layered mafic intrusion, southern Sinai, Egypt: Geologica Acta, v. 14, n. 3, p. 237–259, https://doi.org/10.1344/Geologica Acta2016.14.3.3

Azer, M. K., Gahlan, H. A., Asimow, P. D., and Al-Kahtany, K. M., 2017, The Late Neoproterozoic Dahanib mafic-ultramafic intrusion, South Eastern Desert, Egypt: Is it an Alaskan-type or a layered intrusion?: American Journal of Science, v. 317, n. 8, p. 901–940, https://doi.org/10.2475/08.2017.02

Azer, M. K., Gahlan, H. A., Asimow, P. D., Mubarak, H. S., and Al-Kahtany, K. M., 2019, Multiple stages of carbonation and element redistribution during formation of ultramafic-hosted magnesite in Neoproterozoic ophiolites of the Arabian-Nubian Shield, Egypt: The Journal of Geology, v. 127, n. 1, p. 81–107, https://doi.org/10.1086/700652

Bakor, A. R., Gass, I. G., and Neary, C. R., 1976, Jabal al Wask, northwest Saudi Arabia: An Eocambrian back-arc ophiolite: Earth and Planetary Science Letters, v. 30, n. 1, p. 1–9, https://doi.org/10.1016/0012-821X(76)90002-9

Bernstein, S., Szilas, K., and Kelemen, P. B., 2013, Highly depleted cratonic mantle in West Greenland extending into diamond stability field in the Proterozoic: Lithos, v. 168–169, p. 160–172, https://doi.org/10.1016/j.lithos.2013.02.011

Bonatti, E., and Michael, P. J., 1989, Mantle peridotites from continental rifts to oceanic basins to subduction zones: Earth and Planetary Science Letters, v. 91, p. 297–311, https://doi.org/10.1016/0012-821X(89)90005-8

Borojević Šoštarić, S., Palinkaš, A. L., Neubauer, F., Cvetković, V., Bernroider, M., and Genser, J., 2014, The origin and age of the metamorphic sole from the Rogozna Mts., Western Vardar Belt: New evidence for the one-ocean model for the Balkan ophiolites: Lithos, v. 191–192, p. 39–55, https://doi.org/10.1016/j.lithos.2014.01.011

Boskabadi, A., Pitcairn, I. K., Broman, C., Boyce, A., Teagle, D. A. H., Cooper, M. J., Azer, M. K., Mohamed, F. H., Stern, R. J., and Majka, J., 2017, Carbonate alteration of ophiolitic rocks in the Arabian–Nubian Shield of Egypt: Sources and compositions of the carbonating fluid and implications for the formation of Au deposits: International Geology Review, v. 59, n. 4, p. 391–419, https://doi.org/10.1080/00206814.2016.1227281

Botros, N. S., 2002, Metallogeny of gold in relation to the evolution of the Nubian Shield in Egypt: Ore Geology Reviews, v. 19, n. 3–4, p. 137–164, https://doi.org/10.1016/S0169-1368(01)00035-X

Bourdelle, F., and Cathelineau, M., 2015, Low-temperature chlorite geothermometry: A graphical representation based on a T–R2+–Si diagram: European Journal of Mineralogy, v. 27, n. 5, p. 617–626, https://doi.org/10.1127/ejm/2015/0027-2467

Bruni, J., Canepa, M., Chiodini, G., Cioni, R., Cipolli, F., Longinelli, A., Marini, L., Ottonello, G., and Zuccolini, M. V., 2002, Irreversible water–rock mass transfer accompanying the generation of the neutral, Mg–HCO_3 and high-pH, Ca–OH spring waters of the Genova province, Italy: Applied Geochemistry, v. 17, n. 4, p. 455–474, https://doi.org/10.1016/S0883-2927(01)00113-5

Burkhard, D. J. M., 1993, Accessory chromium spinels: Their coexistence and alteration in serpentinites: Geochimica et Cosmochimica Acta, v. 57, n. 6, p. 1297–1306, https://doi.org/10.1016/0016-7037(93)90066-6

Canovas III, P. A., Hoehler, T., and Shock, E. L., 2017, Geochemical bioenergetics during low-temperature serpentinization: An example from the Samail ophiolite, Sultanate of Oman: Journal of Geophysical Research: Biogeosciences, v. 122, n. 7, p. 1821–1847, https://doi.org/10.1002/2017JG003825

Cathelineau, M., 1988, Cation site occupancy in chlorites and illites as a function of temperature: Clay Minerals, v. 23, n. 4, p. 471–485, https://doi.org/10.1180/claymin.1988.023.4.13

Cathelineau, M., and Nieva, D., 1985, A chlorite solid solution geothermometer. The Los Azufrez (Mexico) geothermal system: Contributions to Mineralogy and Petrology, v. 91, p. 235–244, https://doi.org/10.1007/BF00413350

Clark, I. D., and Fontes, J. C., 1990, Paleoclimatic reconstruction in northern Oman based on carbonates from hyperalkaline groundwaters: Quaternary Research, v. 33, n. 3, p. 320–336, https://doi.org/10.1016/0033-5894(90)90059-T

Coish, R. A., and Gardner, P., 2004, Suprasubduction-zone peridotite in the northern USA Appalachians: Evidence from mineral composition: Mineralogical Magazine, v. 68, n. 4, p. 699–708, https://doi.org/10.1180/0026461046840214

Coleman, R. G., 1977, Ophiolites: Berlin, Germany, Springer-Verlag, Minerals and Rocks, v. 12, 229 p., https://doi.org/10.1007/978-3-642-66673-5

Connolly, J. A. D., 2005, Computation of phase equilibria by linear programming: A tool for geodynamic modelling and its application to subduction zone decarbonation: Earth and Planetary Science Letters, v. 236, n. 1–2, p. 524–541, https://doi.org/10.1016/j.epsl.2005.04.033

Dabitzias, S. G., 1980, Petrology and genesis of the Vavdos cryptocrystalline magnesite deposits, Chalkidiki Peninsula, Northern Greece: Economic Geology, v. 75, n. 8, p. 1138–1151, https://doi.org/10.2113/gsecongeo.75.8.1138

Deer, W. A., Howie, R. A., and Zussman, J., 1992, An introduction to the rock forming minerals, Second Edition: London, England, Longman Scientific and Technical, 712 p.

de Obeso, J. C., and Kelemen, P. B., 2018, Fluid rock interactions on residual mantle peridotites overlain by shallow oceanic limestones: Insights from Wadi Fins, Sultanate of Oman: Chemical Geology, v. 498, p. 139–149, https://doi.org/10.1016/j.chemgeo.2018.09.022

Derbyshire, E. J., O'Driscoll, B., Lenaz, D., Gertisser, R., and Kronz, A., 2013, Compositionally heterogeneous podiform chromitite in the Shetland Ophiolite Complex (Scotland): Implications for chromitite petrogenesis and late-stage alteration in the upper mantle portion of a supra-subduction zone ophiolite: Lithos, v. 162–163, p. 279–300, https://doi.org/10.1016/j.lithos.2012.11.013

Dick, H. J. B., and Bullen, T., 1984, Chromian spinel as a petrogenetic indicator in abyssal and alpine-type peridotites and spatially associated lavas: Contributions to Mineralogy and Petrology, v. 86, n. 1, p. 54–76, https://doi.org/10.1007/BF00373711

Dilek, Y., and Ahmed, Z., 2003, Proterozoic ophiolites of the Arabian Shield and their significance in Precambrian tectonics, *in* Dilek, Y., and Robinson, P. T., editors, Ophiolites in Earth History: Geological Society, London, Special Publications, v. 218, p. 685–700, https://doi.org/10.1144/GSL.SP.2003.218.01.33

Dilek, Y., and Furnes, H., 2011, Ophiolite genesis and global tectonics: Geochemical and tectonic fingerprinting of ancient oceanic lithosphere: GSA Bulletin, v. 123, n. 3–4, p. 387–411, https://doi.org/10.1130/B30446.1

——— 2014, Ophiolites and Their Origins: Elements, v. 10, n. 2, p. 93–100, https://doi.org/10.2113/gselements.10.2.93

Dilek, Y., Furnes, H., and Shallo, M., 2008, Geochemistry of the Jurassic Mirdita Ophiolite (Albania) and the MORB to SSZ evolution of a marginal basin oceanic crust: Lithos, v. 100, n. 1–4, p. 174–209, https://doi.org/10.1016/j.lithos.2007.06.026

Evans, B. W., 1977, Metamorphism of alpine peridotite and serpentinite: Annual Review of Earth and Planetary Sciences, v. 5, n. 1, p. 397–447, https://doi.org/10.1146/annurev.ea.05.050177.002145

Evans, B. W., and Frost, B. R., 1975, Chrome-spinel in progressive metamorphism - a preliminary analysis: Geochimica et Cosmochimica Acta, v. 39, n. 6–7, p. 959–972, https://doi.org/10.1016/0016-7037(75)90041-1

Evans, B. W., and Trommsdorff, V., 1974, Stability of enstatites + talc, and CO_2-metasomatism of metaperidotite, Val d'Efra, Lepontine Alps: American Journal of Science, v. 274, n. 3, p. 274–296, https://doi.org/10.2475/ajs.274.3.274

Falk, E. S., and Kelemen, P. B., 2015, Geochemistry and petrology of listvenite in the Samail ophiolite, Sultanate of Oman: Complete carbonation of peridotite during ophiolite emplacement: Geochimica et Cosmochimica Acta, v. 160, p. 70–90, https://doi.org/10.1016/j.gca.2015.03.014

Falk, E. S., Guo, W., Paukert, A. N., Matter, J. M., Mervine, E. M., and Kelemen, P. B., 2016, Controls on the stable isotope compositions of travertine from hyperalkaline springs in Oman: Insights from clumped isotope measurements: Geochimica et Cosmochimica Acta, v. 192, p. 1–28, https://doi.org/10.1016/j.gca.2016.06.026

Fallick, A. E., Ilich, M., Russell, M. J., 1991, A stable isotope study of the magnesite deposits associated with the Alpine-type ultramafic rocks of Yugoslavia: Economic Geology, v. 86, n. 4, p. 847–861, https://doi.org/10.2113/gsecongeo.86.4.847

Farahat, E. S., and Helmy, H. M., 2006, Abu Hamamid Neoproterozoic Alaskan-type complex, south Eastern Desert, Egypt: Journal of African Earth Sciences, v. 45, n. 2, p. 187–197, https://doi.org/10.1016/j.jafrearsci.2006.02.003

Franz, L., and Wirth, R., 2000, Spinel inclusions in olivine of peridotite xenoliths from TUBAF seamount (Bismarck Archipelago/Papua New Guinea): Evidence for the thermal and tectonic evolution of the oceanic lithosphere: Contributions to Mineralogy and Petrology, v. 140, p. 283–295, https://doi.org/10.1007/s004100000188

Furnes, H., de Wit, M., and Dilek, Y., 2014, Four billion years of ophiolites reveal secular trends in oceanic crust formation: Geoscience Frontiers, v. 5, n. 4, p. 571–603, https://doi.org/10.1016/j.gsf.2014.02.002

Gahlan, H. A., Azer, M. K., and Khalil, A. E. S., 2015, The Neoproterozoic Abu Dahr ophiolite, South Eastern Desert, Egypt: Petrological characteristics and tectonomagmatic evolution: Mineralogy and Petrology, v. 109, p. 611–630, https://doi.org/10.1007/s00710-015-0397-z

Gahlan, H. A., Azer, M. K., and Asimow, P. D., 2018, On the relative timing of listwaenite formation and chromian spinel equilibration in serpentinites: American Mineralogist, v. 103, n. 7, p. 1087–1102, https://doi.org/10.2138/am-2018-6473

Gartzos, E., 2004, Comparative stable isotopes study of the magnesite deposits of Greece: Bulletin of the Geological Society of Greece, v. 36, n. 1, p. 196–203, https://doi.org/10.12681/bgsg.16619

Ghoneim, M. F., Salem, I. A., and Hamdy, M. M., 1999, On the petrogenesis of magnesite from Gebel El-Maiyit, Central Eastern Desert, Egypt: Fourth International Conference on Geology of the Arab World, Cairo University, Egypt, v. 1, p. 575–593.

—— 2003, Origin of magnesite veins in serpentinites from Mount El-Rubshi and Mount El-Maiyit, Eastern Desert, Egypt: Archiwum Mineralogiczne, v. 54, p. 41–63.

Girardeau, J., and Mevel, C., 1982, Amphibolitized sheared gabbros from ophiolites as indicators of the evolution of the oceanic crust: Bay of Islands, Newfoundland: Earth and Planetary Science Letters, v. 61, n. 1, p. 151–165, https://doi.org/10.1016/0012-821X(82)90048-6

Groves, D. I., Goldfarb, R. J., Gebre-Mariam, M., Hagemann, S. G., and Robert, F., 1998, Orogenic gold deposits: A proposed classification in the context of their crustal distribution and relationship to other gold deposit types: Ore Geology Reviews, v. 13, n. 1–5, p. 7–27, https://doi.org/10.1016/S0169-1368(97)00012-7

Habtoor, A. M., Ahmed, A. H., Akizawa, N., Harbi, H., and Arai, S., 2017, Chemical homogeneity of high-Cr chromitites as indicator for widespread invasion of boninitic melt in mantle peridotite of Bir Tuluha ophiolite, Northern Arabian Shield, Saudi Arabia: Ore Geology Reviews, v. 90, p. 243–259, https://doi.org/10.1016/j.oregeorev.2017.03.010

Hadley, D. G., 1987, Geologic map of the Sahl Al Matran quadrangle, sheet 26C, Kingdom of Saudi Arabia: Saudi Arabian Deputy Ministry for Mineral Resources Geoscience Map GM-86, scale 1:250,000.

Hamdy, M. M., and Gamal El Dien, H. M., 2017, Nature of serpentinization and carbonation of ophiolitic peridotites (Eastern Desert, Egypt): Constrains from stable isotopes and whole rock geochemistry: Arabian Journal of Geoscience, v. 10, article n. 429, https://doi.org/10.1007/s12517-017-3215-6

Hamdy, M. M., and Lebda E.M., 2007, Metamorphism of ultramafic rocks at Gebel Arais and Gebel Malo Grim, Eastern Desert, Egypt: Mineralogical and O-H stable isotopic constraints: Egyptian Journal of Geology, v. 51, p. 105–124.

Hart, S. R., and Zindler, A., 1986, In search of a bulk-earth composition: Chemical Geology, v. 57, n. 3–4, p. 247–267, https://doi.org/10.1016/0009-2541(86)90053-7

Hattori, K. H., and Guillot, S., 2007, Geochemical character of serpentinites associated with high- to ultrahigh-pressure metamorphic rocks in the Alps, Cuba, and the Himalayas: Recycling of elements in subduction zones: Geochemistry, Geophysics, Geosystems, v. 8, n. 9, Q09010, https://doi.org/10.1029/2007GC001594

Helmy, H. M., and El Mahallawi, M. M., 2003, Gabbro Akarem mafic-ultramafic complex, Eastern Desert, Egypt: A Late Precambrian analogue of Alaskan-type complexes: Mineralogy and Petrology, v. 77, p. 85–108, https://doi.org/10.1007/s00710-001-0185-9

Hey, M. H., 1954, A new review of the chlorites: Mineralogical Magazine, v. 30, n. 224, p. 272–292, https://doi.org/10.1180/minmag.1954.030.224.01

Hirose, K., and Kawamoto, T., 1995, Hydrous partial melting of lherzolite at 1GPa: The effect of H_2O on the genesis of basaltic magmas: Earth and Planetary Science Letters, v. 133, n. 3–4, p. 463–473, https://doi.org/10.1016/0012-821X(95)00096-U

Holland, T., and Powell, R., 2003, Activity–composition relations for phases in petrological calculations: An asymmetric multicomponent formulation: Contributions to Mineralogy and Petrology, v. 145, n. 4, p. 492–501, https://doi.org/10.1007/s00410-003-0464-z

Holland, T. J. B., and Powell, R., 2011, An improved and extended internally consistent thermodynamic dataset for phases of petrological interest, involving a new equation of state for solids: Journal of Metamorphic Geology, v. 29, n. 3, p. 333–383, https://doi.org/10.1111/j.1525-1314.2010.00923.x

Irvine, T. N., 1965, Chromian spinel as a petrogenetic indicator: Part 1. Theory: Canadian Journal of Earth Sciences, v. 2, n. 6, p. 648–672, https://doi.org/10.1139/e65-046

———— 1967, Chromian spinel as a petrogenetic indicator: Part 2. Petrologic applications: Canadian Journal of Earth Sciences, v. 4, n. 1, p. 71–103, https://doi.org/10.1139/e67-004

Ishii, T., Robinson, P. T., Maekawa, H., and Fiske, R.,1992, Petrological studies of peridotites from diapiric serpentinite seamounts in the Izu-Ogasawara-Mariana forearc, leg 125, *in* Pearce, J., Stokking, L. B., and others, editors, Proceedings of the Ocean-Drilling Project, Leg 125: College Station, Scientific Results, v. 125, p. 445–485, https://doi.org/10.2973/odp.proc.sr.125.129.1992

Jagoutz, E., Palme, H., Baddenhausen, H., Blum, K., Cendales, M., Dreibus, G., Spettel, B., Lorenz, V., and Vanke, H., 1979, The abundance of major, minor and trace elements in the earth's mantle as derived from primitive ultramafic nodules: Geochimica et Cosmochimica Acta, Supplement 11, p. 2031–2050.

Johannes, W., 1970, Zur Entstehung von Magnesitvorkommen: Neues Jahrbuch für Mineralogie Abhandlungen, v. 113, p. 274–325.

Johnson, P. R., and Woldehaimanot, B., 2003, Development of the Arabian-Nubian Shield: Perspectives on accretion and deformation in the northern East African Orogen and the assembly of Gondwana, *in* Yoshida, M., Dasgupta, S., and Windley, B., editors, Proterozoic East Gondwana: Supercontinent assembly and breakup: Geological Society, London ,Special Publications, v. 206, p. 289–325, https://doi.org/10.1144/GSL.SP.2003.206.01.15

Johnson, P. R., Kattan, F. H., and Al-Saleh, A. M., 2004, Neoproterozoic ophiolites in the Arabian Shield: Field relations and structure: Developments in Precambrian Geology, v. 13, p. 129–162., https://doi.org/10.1016/S0166-2635(04)13004-1

Kamenetsky, V. S., Crawford, A. J., and Meffre, S., 2001, Factors controlling chemistry of magmatic spinel: An empirical study of associated olivine, Cr-spinel and meltinclusions from primitive rocks: Journal of Petrology, v. 42, n. 4, p. 655–671, https://doi.org/10.1093/petrology/42.4.655

Kelemen, P. B., and Manning, C. E., 2015, Reevaluating carbon fluxes in subduction zones, what goes down, mostly comes up: Proceedings of the National Academy of Sciences of the United States of America, v.112, n. 30, E3997–E4006, https://doi.org/10.1073/pnas.1507889112

Kelemen, P. B., and Matter, J., 2008, *In situ* carbonation of peridotite for CO_2 storage: Proceedings of the National Academy of Sciences of the United States of America, v. 105, n. 45, p. 17295–17300, https://doi.org/10.1073/pnas.0805794105

Kelemen, P. B., Matter, J., Streit, E. E., Rudge, J. F., Curry, W. B., and Bluztajn, J., 2011, Rates and mechanisms of mineral carbonation in peridotite: Natural processes and recipes for enhanced, *in situ* CO_2 capture and storage: Annual Reviews of Earth and Planetary Sciences, v. 39, p. 545–576, https://doi.org/10.1146/annurev-earth-092010-152509

Kelemen, P. B., Aines, R., Bennett, E., Benson, S. M., Carter, E., Coggon, J. A., De Obeso, J. C., Evans, O., Gadikota, G., Dipple, G. M., Godard, M., Harris, M., Higgins, J. A., Johnson, K. T. M., Kourim, f., Lafay, R., Lambart, S., Manning, C. E., Matter, J. M., Michibayashi, K., Morishita, T., Noël, J., Okazak, K., Renforth, P., Robinson, B., savage, H., Skarbek, R., Spiegelman, M. W., Takazawa, E., Teagle, D., Urai, J. L, Wilcox, J., and the Oman Drilling Project Phase 1 Scientific Party, 2018, *In situ* carbon mineralization in ultramafic rocks: Natural processes and possible engineered methods: Energy Procedia, v. 146, p. 92–102, https://doi.org/10.1016/j.egypro.2018.07.013

Kemp, J., 1981, Geologic map of the Wadi Al 'Ays quadrangle, Sheet 25C, Kingdom of Saudi Arabia: Saudi Arabian Deputy Ministry for Mineral Resources Geologic Map GM 53.

Khalil, A. E. S., Obeid, M. A., and Azer, M. K., 2014, Serpentinized peridotites at the north part of Wadi Allaqi district (Egypt): Implications for the tectono-magmatic evolution of fore-arc crust: Acta Geologica Sinica, v. 88, n. 5, p. 1421–1436, https://doi.org/10.1111/1755-6724.12309

Khedr, M. Z., and Arai, S., 2013, Origin of Neoproterozoic ophiolitic peridotites in south Eastern Desert, Egypt, constrained from primary mantle mineral chemistry: Mineralogy and Petrology, v. 107, p. 807–828, https://doi.org/10.1007/s00710-012-0213-y

Khudeir, A. A., 1995, El-Genina El-Gharbia and El-Genina El-Sharkia ultramafic-mafic intrusions, Eastern Desert, Egypt: geology, petrology, geochemistry and petrogenesis: Assiut, Egypt, Assiut University, Bulletin of Faculty Sciences, Assiut University 2-F, 177–219.

Kimball, K. L., 1990, Effects of hydrothermal alteration on the composition of chromian spinels: Contributions to Mineralogy and Petrology, v. 105, p. 337–346, https://doi.org/10.1007/BF00306543

Klein, F., and Garrido, C. J., 2011, Thermodynamic constraints on mineral carbonation of serpentinized peridotite: Lithos, v. 126, n. 3–4, p. 147–160, https://doi.org/10.1016/j.lithos.2011.07.020

Kranidiotis, P., and MacLean, W. H., 1987, The systematics of chlorite alteration at the Phelps Dodge massive sulfide deposit, Matagami, Quebec: Economic Geology, v. 82, n. 7, p. 1898–1911, https://doi.org/10.2113/gsecongeo.82.7.1898

Kröner, A., Todt, W., Hussein, I. M., Mansour, M., and Rashwan, A. A., 1992, Dating of late Proterozoic ophiolites in Egypt and the Sudan using the single grain zircon evaporation technique: Precambrian Research, v. 59, n. 1–2, p. 15–32, https://doi.org/10.1016/0301-9268(92)90049-T

Kusky, T. M., and Matsah, M. I., 2003, Neoproterozoic dextral faulting on the Najd fault system, Saudi Arabia, preceded sinistral faulting and escape tectonics related to closure of the Mozambique Ocean: Geological Society, London, Special Publications, v. 206, p. 327–61, https://doi.org/10.1144/GSL.SP.2003.206.01.16

Kusky, T. M., and Ramadan, T. M., 2002, Structural controls on Neoproterozoic mineralization in the South Eastern Desert, Egypt:Aan integrated field, Landsat TM, and SIR-C/X SAR approach: Journal of African Earth Sciences, v. 35, n. 1, p. 107–121, https://doi.org/10.1016/S0899-5362(02)00029-5

Launay, J., and Fontes, J. C., 1985, Les sources thermales de Prony (Nouvelle Calédonie) et leurs précipités chimiques, exemple de formation de brucite primaire: Geologie de la France, v. 1, p. 83–100.

Leake, B. E., Woolley, A. R., Arps, C. E. S., Birch, W. D., Gilbert, M. C., Grice, J. D., Hawthorne, F. C., Kato, A., Kisch, H. J., Krivovichev, V. G., Linthout, K., Laird, J., Mandarino, J., Maresch, W. V., Nickel, E. H., Rock, N. M. S., Schumacher, J. C., Smith, D. C., Stephenson, N. C. N., Ungaretti, L., Whittaker, E. J. W., and Youzhi, G., 1997, Nomenclature of amphiboles: Report of the Subcommittee on Amphiboles of the International Mineralogical Association Commission on New Minerals and Mineral Names: European Journal of Mineraligy, v. 9, n. 3, p. 623–651, https://doi.org/10.1127/ejm/9/3/0623

Leake, B. E., Woolley, A. R., Birch, W. D., Burke, E. A. J., Ferraris, G., Grice, J. D., Hawthorne, F. C., Kisch, H. J., Krivovichev, V. G., Schumacher, J. C., Stephenson, N. C. N., and Whittaker, E. J. W., 2004, Nomenclature of amphiboles: Additions and revisions to the International Mineralogical Association's amphibole nomenclature: European Journal of Mineralogy, v. 16, p. 190–195, https://doi.org/10.1127/0935-1221/2004/0016-0191

Ledru, P., and Auge, T., 1984, The Al Ays ophiolitic complex; petrology and structural evolution: BRGM-OF-04-15, Saudi Arabia Deputy Ministry for Mineral Resources.

McDonough, W. F., and S.-s. Sun, 1995, The Composition of the Earth: Chemical Geology, v. 120, n. 3–4, p. 223–53, https://doi.org/10.1016/0009-2541(94)00140-4

Mellini, M., Rumori, C. and Viti, C., 2005, Hydrothermally reset magmatic spinels in retrograde serpentinites: Formation of "ferritchromit" rims and chlorite aureoles: Contributions to Mineralogy and Petrology, v. 149, p. 266–275, https://doi.org/10.1007/s00410-005-0654-y

Menzel, M. D., Garrido, C. J., Sánchez-Vizcaíno, V. L., Marchesi, C., Hidas, K., Escayola, M. P., and Huertas, A. D., 2018, Carbonation of mantle peridotite by CO_2-rich fluids: The formation of listvenites in the Advocate ophiolite complex (Newfoundland, Canada): Lithos, v. 323, p. 238–261, https://doi.org/10.1016/j.lithos.2018.06.001

Nassief, M. O., Macdonald, R., and Gass, I. G., 1984, The Jabal Thurwah upper Proterozoic ophiolite complex, western Saudi Arabia: Journal of the Geological Society, London, v. 141, n. 3, p. 537–546, https://doi.org/10.1144/gsjgs.141.3.0537

Neary, C. R., and Brown, M., 1979, Chromites from Al Ays complex, Saudi Arabia and the Semail complex, *in* Al Shanti, A. M. S., editor, Evolution and Mineralization of the Arabian Shield: Institution of American Geologists Bulletin, v. 2, p. 193–205, https://doi.org/10.1016/B978-0-08-024467-9.50022-8

Nehlig, P., Genna, A., and Asfirane, F., 2002, A review of the Pan-African evolution of the Arabian Shield: GeoArabia, v. 7, n. 1, p. 103–124.

Niu, Y., 2004, Bulk-rock major and trace element compositions of abyssal peridotites: Implications for mantle melting, melt extraction and post-melting processes beneath mid-ocean ridges: Journal of Petrology, v. 45, n. 12, p. 2423–2458, https://doi.org/10.1093/petrology/egh068

Obeid, M. A., Khalil, A. E. S., and Azer, M .K., 2016, Mineralogy, geochemistry and geotectonic significance of the Neoproterozoic ophiolite of Wadi Arais area, south Eastern Desert, Egypt: International Geology Review, v. 58, n. 6, p. 687–702, https://doi.org/10.1080/00206814.2015.1105727

Oskierski, H. C., Bailey, J. G., Kennedy, E. M., Jacobsen, G., Ashley, P. M., and Dlugogoski, B. Z., 2013, Formation of weathering-derived magnesite deposits in the New England Orogen, New South Wales, Australia: Implications from mineralogy, geochemistry and genesis of the Attunga magnesite deposit: Mineralium Deposita, v. 48, p. 525–541, https://doi.org/10.1007/s00126-012-0440-5

Pallister, J. S., Stacey, J. S., Fischer, L. B., and Premo, W. R., 1988, Precambrian ophiolites of Arabia: Geologic settings, U-Pb geochronology, Pb-isotope characteristics, and implications for continental accretion: Precambrian Research, v. 38, n. 1, p. 1–54, https://doi.org/10.1016/0301-9268(88)90092-7

Parkinson, I. J., and Pearce, J. A., 1998, Peridotites from the Izu-Bonin- Mariana forearc (ODP Log 125): Evidence for mantle melting and melt-mantle interaction in a supra-subduction zone setting: Journal of Petrology, v. 39, n. 9, p. 1577–1618, https://doi.org/10.1093/petroj/39.9.1577

Pearce, J. A., Lippard, S. J., and Roberts, S., 1984, Characteristics and tectonic significance of supra-subduction zone ophiolites, *in* Kokelaar, P. B., and Howells, M. F., editors, Marginal basin geology: Geological Society of London, Special Publications, v. 16, p. 77–94, https://doi.org/10.1144/GSL.SP.1984.016.01.06

Pearce, J. A., Barker, P. F., Edwards, S. J., Parkinson, I. J., and Leat, P. T., 2000, Geochemistry and tectonic significance of peridotites from the South Sandwich arc-basin system, South Atlantic: Contributions to Mineralogy and Petrology, v. 139, p. 36–53, https://doi.org/10.1007/s004100050572

Penrose Conference Participants, 1972, Report of the Penrose field conference on ophiolites: Geotimes, v. 17, p. 24–25.

Petriglieri, J. R., Salvioli-Mariani, E., Mantovani, L., Tribaudino, M., Lottici, P. P., Laporte-Magoni, C., and Bersani, D., 2015, Micro-Raman mapping of the polymorphs of serpentine: Journal of Raman Spectroscopy, v. 46, n. 10, p. 953–958, https://doi.org/10.1002/jrs.4695

Pitzer, K. S., and Sterner, S. M., 1994, Equations of state valid continuously from zero to extreme pressures for H_2O and CO_2: The Journal of Chemical Physics, v. 101, n. 4, p. 3111–3116, https://doi.org/10.1063/1.467624

Power I. M., Wilson S. A., and Dipple G. M., 2013, Serpentinite carbonation for CO_2 sequestration: Elements, v. 9, n. 2, p. 115–121, https://doi.org/10.2113/gselements.9.2.115

Qiu, R. Z., Zhou, S., Li, T. D., Deng, J. F., Xiao, Q. H., Wu, Z. X., and Cai, Z. Y., 2007, The tectonic-setting of ophiolites in the western Qinghai-Tibet Plateau, China: Journal of Asian Earth Sciences, v. 29, n. 2–3, p. 215–228, https://doi.org/10.1016/j.jseaes.2006.06.007

Quesnel, B., Gautier, P., Boulvais, P., Cathelineau, M., Maurizot, P., Cluzel, D., Ulrich, M., Guillot, S., Lesimple, S., and Couteau, C., 2013, Syn-tectonic, meteoric water-derived carbonation of the New Caledonia peridotite nappe: Geology, v. 41, n. 10, p. 1063–1066, https://doi.org/10.1130/G34531.1

Quick, J. E., 1990, Geology and origin of the late Proterozoic Darb Zubaydah ophiolite, Kingdom of Saudi Arabia: GSA Bulletin, v. 102, n. 8, p. 1007–1020, https://doi.org/10.1130/0016-7606(1990)102<1007: GAOOTL>2.3.CO;2

Salem, I. A., Ghoneim, M. F., Zahran, A. A., and Hamdy, M. M., 1997, Petrology and genesis of the ultramafic-hosted vein magnesite deposits at G. El-Rubshi, central Eastern Desert, Egypt: 3rd International Conference on Geochemistry, Alexandria University, Alexandria-Egypt, p. 241–267

Scarsi, M., Malatesta, C., and Fornasaro, S., 2018, Lawsonite-bearing eclogite from a tectonic mélange in the Ligurian Alps: New constraints for the subduction plate-interface evolution: Geological Magazine, v. 155, n. 2, p. 280–297, https://doi.org/10.1017/S0016756817000395

Shukri, N. M., and Lotfi, M., 1959, The Geology of the Bir Barramiya area: Bulletin of Faculty of Science, Cairo University, v. 34, p. 83–130.

Skelton, A., 2011, Flux rates for water and carbon during greenschist facies metamorphism. Geology, v. 39, n. 1, p. 43–46, https://doi.org/10.1130/G31328.1

Stern, R. J., 1985, The Najd Fault System, Saudi Arabia and Egypt: A late Precambrian rift-related transform system: Tectonics, v. 4, n. 5, p. 497–511, https://doi.org/10.1029/TC004i005p00497

——— 1994, Arc assembly and continental collision in the Neoproterozoic East African Orogen: Implications for the consolidation of Gondwanaland: Annual Review of Earth and Planetary Sciences, v. 22, p. 319–351, https://doi.org/10.1146/annurev.ea.22.050194.001535

Stern, R. J., and Gwinn, C. J., 1990, Origin of Late Precambrian intrusive carbonates, Eastern Desert of Egypt and Sudan: C, O, and Sr isotopic evidence: Precambrian Research, v. 46, n. 3, p. 259–272, https://doi.org/10.1016/0301-9268(90)90005-B

Stern, R. J., Nielsen, K. C., Best, E., Sultan, M., Arvidson, R. E., and Kröner A., 1990, Orientation of late Precambrian sutures in the Arabian-Nubian Shield: Geology, v. 18, n. 11, p. 1103–1106, https://doi.org/10.1130/0091-7613(1990)018<1103:OOLPSI>2.3.CO;2

Stern, R. J., Johnson, P. R., Kröner, A., and Yibas, B., 2004, Neoproterozoic ophiolites of the Arabian-Nubian Shield, *in* Kusky, T. M., editor, Precambrian Ophiolites and Related Rocks: Developments in Precambrian Geology, v. 13, p. 95–128, https://doi.org/10.1016/S0166-2635(04)13003-X

Streckeisen, A., 1976, To each plutonic rock its proper name: Earth-Science Reviews, v. 12, n. 1, p. 1–33, https://doi.org/10.1016/0012-8252(76)90052-0

Suita, M., and Strieder, A., 1996, Cr-spinels from Brazilian mafic-ultramafic complexes: Metamorphic modifications: International Geology Review, v. 38, n. 3, p. 245–267, https://doi.org/10.1080/00206819709465333

Takahashi, E., Uto, K., and Schilling, J. G., 1987, Primary magma compositions and Mg/Fe ratios of their mantle residues along mid-Atlantic ridge 29N to 73N: Technical Report, A9, Institute of Studies Earth's Interior, Okayama University Series, p. 1–14.

Uysal, I., Yalçın Ersoy, E., Karsli, O., Dilek, Y., Burhan Sadiklar, M., Ottley, C. J., Tiepolo, M., and Meisel, T., 2012, Coexistence of abyssal and ultra-depleted SSZ type mantle peridotites in a Neo-Tethyan Ophiolite in SW Turkey: Constraints from mineral composition, whole-rock geochemistry (major-trace-REE-PGE), and Re-Os isotope systematic: Lithos, v. 132–133, p. 50–69, https://doi.org/10.1016/j.lithos.2011.11.009

Yavuz, F., Kumral, M., Karakaya, N., Karakaya, M.C., and Yildirim, D. K., 2015, A Windows program for chlorite calculation and classification: Computers and Geosciences, v. 81, p. 101–113, https://doi.org/10.1016/j.cageo.2015.04.011